AD-A118 553 CALIFORNIA UNIV LOS ANGELES DEPT OF MATERIALS SCIEN--ETC F/G 11/6
FUNDAMENTAL INVESTIGATION OF THE RETROGRESSION AND REAGING (RRA--ETC(U)
MAY 82 A J ARDELL, J K PARK N00014-81-K-0292

UNCLASSIFIED NL

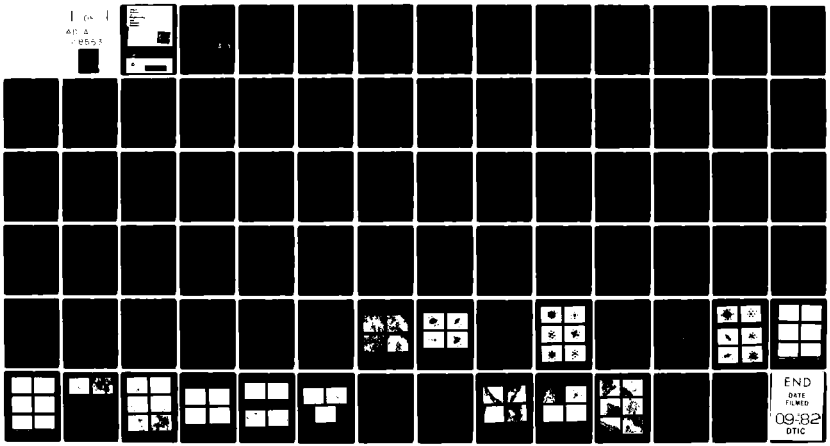

UCLA School of Engineering and Applied Science

FIRST ANNUAL PROGRESS REPORT May 1982

A. J. Ardell and J. K. Park
Materials Science and
Engineering Department
University of California
Los Angeles, CA 90024

FUNDAMENTAL INVESTIGATION OF THE RETROGRESSION AND REAGING (RRA) OF COMMERCIAL Al-BASE ALLOYS AND ITS EFFECT ON STRESS CORROSION CRACKING

Contract No. N00014-81-K-0292
NR 036-140

SECURITY CLASSIFICATION OF THIS PAGE (When Data Entered)

REPORT DOCUMENTATION PAGE

READ INSTRUCTIONS BEFORE COMPLETING FORM

1. REPORT NUMBER
TECHNICAL REPORT

2. GOVT ACCESSION NO. A118553

3. RECIPIENT'S CATALOG NUMBER

4. TITLE (and Subtitle)
Fundamental Investigation of the Retrogression and Reaging (RRA) of Commercial Aℓ-Base Alloys and Its Effect on Stress Corrosion Cracking

5. TYPE OF REPORT & PERIOD COVERED
ANNUAL PROGRESS REPORT
March 1, 1981-Feb. 28, 1982

6. PERFORMING ORG. REPORT NUMBER

7. AUTHOR(s)
A.J. Ardell and J.K. Park

8. CONTRACT OR GRANT NUMBER(s)
N00014-81-K-0292

9. PERFORMING ORGANIZATION NAME AND ADDRESS
Department of Materials Science & Engineering
University of California
Los Angeles, CA 90024

10. PROGRAM ELEMENT, PROJECT, TASK AREA & WORK UNIT NUMBERS

11. CONTROLLING OFFICE NAME AND ADDRESS
MATERIALS DIVISION
OFFICE OF NAVAL RESEARCH
ARLINGTON, VA 22217

12. REPORT DATE
May 26, 1982

13. NUMBER OF PAGES
79

14. MONITORING AGENCY NAME & ADDRESS(if different from Controlling Office)

15. SECURITY CLASS. (of this report)

15a. DECLASSIFICATION/DOWNGRADING SCHEDULE

16. DISTRIBUTION STATEMENT (of this Report)
Distribution is unlimited

17. DISTRIBUTION STATEMENT (of the abstract entered in Block 20, if different from Report)

18. SUPPLEMENTARY NOTES

19. KEY WORDS (Continue on reverse side if necessary and identify by block number)
Precipitation reactions, transmission electron microscopy, retrogression and reaging heat treatments, matrix and grain boundary microstructures

20. ABSTRACT (Continue on reverse side if necessary and identify by block number)
The microstructure of 7075 Aℓ, aged to the T6 and T76 temper conditions, has been carefully characterized with respect to the nature of the precipitate phases that exist in the matrix and in grain boundaries, and the parameters associated with their dispersions. The microstructural changes that occur during various retrogression and retrogression and reaging heat-treatments have been thoroughly documented. The possible consequences of these latter heat treatments on the stress-corrosion susceptibility and yield strength of Aℓ 7075 are discussed.

DD FORM 1 JAN 73 1473

SECURITY CLASSIFICATION OF THIS PAGE (When Data Entered)

I. Introduction

I - 1. Aging Characteristics of Aℓ-Zn-Mg Alloys

The precipitation process during the aging of Aℓ-Zn-Mg alloys has been the subject of extensive research due to the technical importance of this system. Much of the effort has been concentrated on the determination of microstructure, such as the type, morphology, distribution and crystallography of the precipitates resulting from the aging sequence to understand the role of microstructure in strengthening and stress corrosion cracking resistance.

Most of the microstructural work has been done on pure Aℓ-Zn-Mg alloys. Earlier results deduced from x-ray studies [1-6] revealed the existence of solute rich clusters, spherical G.P. zones and the transition phase η'. The aging sequence at temperatures below 190°C is generally proposed as:[7-8]

α supersaturated solid solution $\rightarrow$ G.P. zones $\rightarrow \eta' \rightarrow \eta$

The equilibrium η phase, $MgZn_2$ has the hexagonal structure, with a = 5.21 Å and c = 8.60 Å [9]. Nine different orientation relationships with the matrix have been reported. In the classification scheme of Simensen et al. [10] they are:

* Type 1: $(10.0)_{\eta_1} \parallel (001)_{A\ell}$; $(00.1)_{\eta_1} \parallel (110)_{A\ell}$ [6]

Type 2: $(00.1)_{\eta_2} \parallel (1\bar{1}\bar{1})_{A\ell}$; $(10.0)_{\eta_2} \parallel (110)_{A\ell}$ [6]

Type 3: $(00.1)_{\eta_3} \parallel (1\bar{1}\bar{1})_{A\ell}$; $(11.0)_{\eta_3} \parallel (110)_{A\ell}$ [6]

Type 4: $(00.1)_{\eta_4} \parallel (110)_{A\ell}$; $(\bar{1}2.0)_{\eta_4} \parallel (1\bar{1}\bar{1})_{A\ell}$ [11]

Type 5: $(\bar{1}2.0)_{\eta_5} \parallel (1\bar{1}\bar{1})_{A\ell}$; $(30.2)_{\eta_5} \parallel (110)_{A\ell}$[11]

Type 6: $(\bar{1}2.0)_{\eta_6} \parallel (1\bar{1}\bar{1})_{A\ell}$; $(20.1)_{\eta_6} \parallel (1\bar{1}2)_{A\ell}$[11]

Type 7: $(\bar{1}2.0)_{\eta_7} \parallel (1\bar{1}\bar{1})_{A\ell}$; $(10.4)_{\eta_7} \parallel (110)_{A\ell}$[11]

Type 8: $(\bar{1}2.0)_{\eta_8} \parallel (1\bar{1}2)_{A\ell}$; $(00.1)_{\eta_8} \parallel (31\bar{1})_{A\ell}$[10]

Type 9: $(\bar{1}2.0)_{\eta_9} \parallel (001)_{A\ell}$; $(00.1)_{\eta_9} \parallel (110)_{A\ell}$[12]

* The term 'type' implies the family of at least 6 variants belonging to the given orientation relationship of the η phase. In this report, the term 'variant' has the same meaning as the term 'type.'

However, three types, η_1, η_2 and η_4 have been reported to be the most frequently observed phases among the nine types of η phases at intermediate aging temperatures (usually 75 to 150°C)[10,11]. It is also known that η_1 and η_2 are plate-shaped and that the η_4 type has a lath type morphology[11]. In addition the T phase $(A\ell Zn)_{49}\,Mg_{32}$ can be formed above ~ 190°C; it has a cubic structure with a = 14.16 Å[6].

Spherical G.P. zones are usually the first decomposition product near the composition $A\ell$-$MgZn_2$ at low temperature (usually $\leq$ 75°C). Graf[3] and Schmalzried and Gerold[6] have found that there are additional steps in the aging sequence for certain alloys. Their x-ray results indicated that G.P. zones become ordered with Zn and Mg atoms on alternate {100} planes in an intermediate aging temperature range (usually 75 to 150°C) (this is sometimes referred to as η''[8]. Mondolfo et al.[1] suggested that at temperatures below 200°C the initial G.P. zone formation is followed by the formation of the η' transition phase of hexagonal structure, with a = 4.96 Å, c = 8.68 Å. On the other hand, Graf [5] suggested that a coherent hexagonal transition

phase, η' forms in the intermediate aging temperature range. Graf[5] reported its lattice constants as a = 4.96 Å and c = 14.03 Å, which are different from those of Mondolfo et al. Graf[2,4] also found that G.P. zones are the initial decomposition product only during aging in the low temperature range (below ~ 75°C). Increasing the aging temperature to the range 100 to 130°C leads to the initial formation of the η' transition phase without evidence of G.P. zone formation.

More recent studies by transmission electron microscopy have yielded additional information on the details of the aging process[10-14]. Lorimer and Nicholson[7,15], in their general model of two-step aging, proposed that G.P. zones act as nuclei for the formation of the η' transition phase. On the other hand, Pashley et al.[16] proposed that the η' transition phase can be formed directly from stable clusters, implying that G.P. zones are not necessarily a precursor to the formation of η' precipitates. Thackery[11] could not find evidence of the η' transition phase in his study on an Aℓ-6Zn-2Mg alloy, and suggested that G.P. zones transformed directly to the equilibrium η phase. Gjønnes and Simensen [10] in their study on Aℓ-5.8Zn-1.1Mg, however, found that the coherent transition phase η' forms in the form of plates on {111}, as suggested earlier by Thomas and Nutting[14], during aging at 130°C and 150°C. They described its structure as having a monoclinic unit cell with, a = b = 4.97 Å, c = 5.54 Å and γ = 120°, with the orientation relationship $(00.1)_{\eta'} || (1\bar{1}\bar{1})_{A\ell}$; $(10.0)_{\eta'} || (110)_{A\ell}$. Subsequent x-ray work by Auld et al.[17], however, identified the η' phase as having a hexagonal structure, confirming earlier x-ray work, but with different lattice parameters, a = 4.89 Å, c = 13.74 Å. Gjønnes and Simensen[10] further observed small spherically shaped particles, together with plate-shaped η' particles at an early stage of aging; these were found to be responsible for streaks

parallel to $\langle 111 \rangle_{A\ell}$ in the diffraction pattern. They interpreted the small spherically shaped particles as another form of the η' transition phase. Somewhat earlier, Embury and Nicholson[12] observed similar small spherically shaped particles. However they considered them as ordered G.P. zones. Gjønnes and Simensen [10] further reported that they could not find any evidence of G.P. zone formation during the early stages of aging. Subsequent studies of the effects of 2-stage heat treatments by DeArdo and Simensen[12] confirmed the results of Gjønnes and Simensen[10]. In addition, they[10,12] observed that one of the η variants, the η_1 type, is present together with the η' transition phase at an early stage of aging at 100°C, and that the η' phase transforms mainly to one of the η variants, the η_2 type, during aging at 180°C. On the basis of such findings, they suggested that the G.P. zones are not necessarily the precursor to the formation of the η' transition phase at the aging temperatures 100°C and 180°C. Hence the η_1 type as well as the η' transition phase, can be directly formed from the supersaturated solid solution without any preceeding G.P. zone formation. Ryum[18] also obtained similar results, and suggested two possible types of nuclei for the precipitates, i.e., solute rich clusters (not necessarily G.P. zones), similar to the concept of Pashley et al.[16], and vacancy-rich clusters. Lyman and Vander Sande[19] studied recently the early stages of precipitation using high resolution electron microscopy. They also observed coherent small spherical particles before the onset of plate-like η' precipitates at intermediate aging temperatures (70 to 100°C) and suggested that they would be a spherical precursor of the η' transition phase having the η' structure. They considered, however, such particles to be spherical ordered hexagonal zones rather than η' phases themselves. It may be worth mentioning that recent

knowledge about G.P. zones, such as their formation and reversion kinetics and thermal stability, has been essentially deduced from indirect experiments, such as the earlier x-ray studies[1-6], many recent x-ray small angle scattering studies[20,21], sometimes in conjunction with differential scanning calorimetric measurements[22] and studies using resistivity measurements[23]. The above discussions reveal that there appears to be some controversy in the literature on the aging sequence, particularly on the exact nature of G.P. zones and the η' transition phase.

It is well known that age-hardenable Aℓ alloys exhibit precipitate free zones (PFZ) adjacent to the grain boundaries[7, 15, 16]. It was originally thought that the formation of PFZs is due to the local depletion of solute atoms near grain boundaries as a result of the formation of grain boundary precipitates. However, Nicholson and his co-workers[7,15], demonstrated that PFZs can also form as a result of a depletion of lattice vacancies near grain boundaries due to the migration of vacancies to them.

Concerning the characteristic microstructure responsible for the precipitation hardening of Aℓ-Zn-Mg alloys, Thomas and Nutting[14] suggested that hardness is a function only of the degree of dispersion of the precipitates (the smaller the interparticle spacing, the higher the hardness) regardless of the precipitate types or their degree of coherency. DeArdo and Simensen[13] suggest in a similar manner that a fine distribution of both the η' and η phases is responsible for maximum hardness. Nicholson et al.[24] found that age hardening was related to a dispersion hardening mechanism due to η' plates. Meanwhile, Kelly and Nicholson[25] observed that the microstructure at peak hardness contained mainly the η' phase. Gjønnes and Simensen[10] found a close correlation between the time development of η' particles and measured hardness and suggested that a fine dispersion of the semi-coherent η' plates is mainly

responsible for higher hardness.

Only recently, a few attempts have been made to quantitatively correlate the microstructure to the yield stress in Aℓ-Zn-Mg alloys[26,27]. This may be partly due to the complex precipitation process that occurs in the Aℓ-Zn-Mg system as described previously; particle sizes are usually small until well beyond peak hardness, and their morphologies are usually plate-shaped rather than spherical, except at very early stages of aging. Also, several phases are simultaneously present at all aging temperatures. Melander et al.[26] reported that the results of the correlation between their theoretical strengthening model and the measured particle size distribution can be interpreted in terms of a model for shear modulus hardening for small particles (they are referred to as G.P. zones) and that the Orowan mechanism is effective for coarser incoherent particles (called the η phase).

Few studies have so far been done in detail on the characterization of the microstructure of precipitation-hardened commercial 7000 series alloys. Adler and DeIasi recently studied the microstructure of Aℓ 7075 using TEM in an attempt to correlate it to its SCC susceptibility[28], and to the results of differential scanning calorimetric (DSC) measurements[29,30]. They reported that G.P. zones are the predominant precipitates in the maximum hardness (T651) condition, while in the T73 condition the microstructure mainly consists of the η' transition phase. However, this result apparently appears to contradict the results on pure Aℓ-Zn-Mg alloys discussed above. The technique used by Adler and DeIasi for the identification of the nature of the precipitates is not clear in their report; they reported that the identification of the precipitates was simply based on consideration of size and observation of the morphology of the precipitates. Recently, Papazian[31] studied the DSC characteristics of Aℓ 7075 in various aging conditions, but no detailed microstructural study was made.

I-2 SCC vs. Microstructure of Aℓ-Zn-Mg Alloys

It is well known that commercial 7000 series Aℓ alloys are subject to intergranular stress corrosion cracking (SCC) depending upon the aging conditions; maximum strength 7075-T6 is the most susceptible to SCC, while overaged 7075-T7X is very resistant to SCC[32,33]. However, overaging leads to a 10 to 20% sacrifice of its strength, depending upon the dimensions of the material. Intergranular stress corrosion is closely related to the microstructure as well as the microchemistry near grain boundaries. Many investigators have studied the microstructure near grain boundaries, and recently, the microchemistry near grain boundaries in an attempt to correlate them with the susceptibility of these alloys to SCC.

Dix and co-workers[34-36] originally found that η ($MgZn_2$) grain boundary precipitates are anodic to the matrix and suggested that they act as preferential dissolution sites. Further careful electrochemical studies by Sedriks et al.[37,38] confirmed this result. Based upon this fact, many investigators have considered the sites of dissolved η phases as the opening of fissures necessary for later crack propagation, and have predicted that the susceptibility to SCC would increase with increased coverage of η on the grain boundaries[34-40].

However, a somewhat different point of view on the role of electrochemically active η phases has been recently expressed by Morral and McEvily et al.[41,42]. In their study on the relationship between microstructure and steady-state SCC velocity[41], they found that the steady-state crack velocity

decreased with increasing line fraction of grain boundary precipitates, and also with the decreasing number density of grain boundary precipitates which results from overaging. On the basis of such experimental findings, they suggested that grain boundary precipitates would act as sacrificial anodes instead of crack initiation sites, thereby decreasing the SCC velocity, Peel et al.[43] observed also that line fraction of grain boundary precipitates increases as alloys become overaged, and agreed with McEvily et al.'s point of view.

Meanwhile Kent[40 44], Adler et al.[28] and Rao[45] also observed that as the aging time increases, the number of grain boundary precipitates decreases and hence the interparticle spacing also increases. However, they attributed the good resistance of the overaged alloy to this wider interparticle spacing on grain boundaries rather than to increasing coverage by precipitates resulting from overaging, confirming Dix et al.'s point of view.

Many earlier investigators have tried to correlate the PFZ width with the SCC susceptibility[46,47]. However, recent work indicates that no definite trend between lifetime and PFZ width can be found[28,40,41,48]. Recently, Doig and Edington[49-52], Ward and Lorimer[53] and Raghavan[54] measured solute concentration profiles across the PFZ, either by analysis of electron energy loss or by x-ray energy dispersive spectrometry (EDS) in the electron microscope. Their results suggest that the solute distribution would have a more important role on SCC susceptibility than the PFZ width itself. Doig and Edington[49,51,52] measured the concentration profile across the PFZ by monitoring the plasmon losses of transmitted electrons in an as-quenched, peak-aged and overaged Aℓ-Zn-Mg alloy. They found an accumulation of Mg in as-quenched Aℓ-5.5% Zn - 3.2% Mg and a depletion of Mg in the overaged condition at the grain boundary; this was interpreted as due to the fact that overaging caused most of the Mg at grain boundaries to combine to form the η phases, thus leaving the region between

precipitates depleted in Mg.

Recent results using Auger spectroscopy [55-57] appear to indicate that Mg segregates to grain boundaries in amounts in excess of the Mg associated with η phases in all aging conditions (even in the overaged condition). Green et al.[55,58] found marked segregation of Mg and Zn to the grain boundaries in both as-quenched and overaged Aℓ-5.5%Zn-2.5%Mg. About 60% of the total at the grain boundaries was segregated as free Mg to within a few atomic distances of the grain boundary, while the remaining Mg was incorporated in G.B. precipitates. The implication of the observed segregation of Mg to SCC was interpreted as a possible Mg-H complex formation, which would result in hydrogen embrittlement. Some experimental evidence that hydrogen embrittlement could be a controlling mechanism for intergranular stress corrosion crack propagation in high strength Aℓ alloys has been recently presented by Troiano[59], Swann[60], Speidel[61], Scamans[62] and their co-workers.

I - 3 Retrogression and Reaging Heat Treatment

The above review of the literature reveals that there is still some controversy over the fundamental parameters responsible for stress corrosion cracking in Aℓ-Zn-Mg alloys. The overaging heat treatment T7x has been conventionally applied to reduce the susceptibility of Aℓ-7075 to SCC. However, this heat-treatment necessarily sacrifices its maximum strength. Cina and Ranish[63] and Cina[64,65] recently proposed a new heat treatment, called a Retrogression and Reaging (RRA) treatment[66], which substantially increases the resistance to SCC of Aℓ-7075 without sacrificing the maximum strength of the T6 condition. The RRA heat treatment consists of a short time (usually the order of ten seconds) retrogression treatment on alloys in the T6 temper in the annealing temperature range within the two phase region, followed by water quenching and a final reaging treatment at 120°C, the temperature of the original T6 temper. Subsequent research by Lockheed[66] confirmed the findings of Cina and Ranish;

they demonstrated that the RRA treatment increases the threshold stress for SCC by several times over that of 7075-T6, and that more than 95% of the maximum T6 hardness was restored after the RRA treatment. Furthermore, exfoliation is eliminated as a reuslt of the RRA treatment. Lockheed[66] further demonstrated that the RRA treatment can be applied in a practical manner to a variety of structural members fabricated by forging, such as engine mount trusses and steering collars. In all cases, the RRA treatment greatly improved the resistance of Aℓ 7075-T6 to SCC without no significant reduction of its tensile properties. The RRA heat treatment has become potentially important in the aerospace industry recently as a possible method of reducing the susceptibility to SCC, with no loss of strength, of in-service aircraft parts made of Aℓ 7075-T6, hence conserving both materials and energy[67-69].

It may be worth mentioning, however, that very recent results of SCC testing[70] seem to suggest that the RRA treatment does not enchance significantly the resistance to the notch-sensitive stress corrosion cracking of Aℓ 7075-T6. Very recently Papazian[31] measured the thermal behavior of Aℓ 7075 in the T6, T73 and RRA conditions using DSC and reported that the dissolution characteristics of RRA conditions are rather similar to those of the T73 condition. However, the mechanism responsible for the beneficial effect of the RRA treatment on Aℓ 7075-T6 (in unnotched specimens) remains unknown, since the importance of the RRA treatment has been recognized only recently.

I-4 Purpose of Present Research

Since the SCC susceptibility as well as the strength of Aℓ-Zn-Mg alloys are intrinsically related to the microstructure of both the matrix and grain boundaries, and to the microchemistry near grain boundaries, it is

believed that a true understanding of the beneficial effect of the RRA heat treatment on Aℓ 7075-T6 can only be derived from a detailed study of both the microstructure and microchemistry of the RRA-treated alloy. It is first required to have detailed information on both the microstructure and microchemistry of the alloy in the peak-aged (T6) and overaged (T76) tempers. However, such information is not so far available, as described previously; i.e., in pure Aℓ-Zn-Mg alloys, there appears to be some controversy over the nature of the small spherical particles that form during the early stages of aging, whether they are G.P. zones, ordered hexagonal zones (η'') or the η' phase. Also, the exact nature of the η' transition phase is not well-established. The ambiguity becomes more serious when the commercial Aℓ 7075 alloy is considered due to the absence of detailed microstructural work on it. Concerning the microstructure of precipitates on grain boundaries in Aℓ-Zn-Mg alloys in relation to the susceptibility to SCC, it is generally agreed that the coarsening of G.B. particles decreases the susceptibility to SCC. However, the exact role of G.B. particles on the propagation of stress corrosion cracks is not well established. The role of the PFZ on the susceptibility to SCC appears to be contradictory. Recent results, however, seem to indicate that the microchemistry within the PFZ plays a more important role on the susceptibility to SCC than the width of the PFZ. Also the importance of microsegregation to the G.B. area has become increasingly emphasized, particularly in connection with hydrogen embrittlement as a fundamental mechanism of SCC, as opposed to an anodic dissolution theory.

The present research consists of two main purposes; the first is to study in detail the effect of the RRA treatment on the microstructure of commercial Aℓ 7075-T6, in both the matrix and grain boundary regions using the transmission electron microscope. The microstructure of commercial Aℓ 7075

alloy in both the peak-aged (T6) and overaged (T76) tempers will be first characterized in detail for that purpose. The other consists of investigating the microchemistry within the PFZ, as well as on grain boundaries, of RRA trated Aℓ 7075, using STEM and EDS. This will be also accompanied by a detailed microchemical investigation of the near-grain-boundary regions of Aℓ 7075 in both peak-aged and overaged conditions. The following presents the results of the microstructural research.

II. Experimental Procedures

The material used in this study is extruded commercial Aℓ 7075 in the T651 condition. It was received from Lockheed in the form of bar 3 x 10 x 110 cm. ST-L sections were cut into thin strips 0.25mm in thickness using a spark cutting machine. Some L-T sections were also cut to study the orientation dependence of the microstructure. The strips were used for the subsequent heat-treatments and for the preparation of thin films for electron microscopy.

The retrogression heat-treatment was performed in a salt bath at 240 ± 2°C, which is the optimum retrogression temperature according to previous work[63,66]. The strips were retrogressed for various times up to 60s and water-quenched to room temperature. Reaging was done immediately after the retrogression treatment at 120 ± 1°C in a stirred oil both for 48 hr. Some of the retrogressed strips were kept at 0°C after the heat-treatment to prevent further possible natural aging.

For the purpose of determining the optimum retrogression time microhardness was measured as a function of retrogression time before and after the reaging treatment. Five disks 3mm in dia. were punched from each strip specimen. After having polished them mechanically to remove the damage due to spark machining, the disks were further polished electrolytically to produce a final smooth surface. The final thickness of the disks was in the range 0.10 to 0.17mm. The Knoop hardness at 100gm load was measured, nine measurements taken on each disk. For hardness measurements on the retrogressed strips, particular precaution was taken to minimize possible room temperature aging. All the samples were kept at 0°C, except during mechanical polishing and hardness measurement, the total estimated time of which was about 30 min.

Samples were heat-treated to the T76 temper in order to compare the microstructure and microchemistry with those of RRA treated specimens. Strips in the T651 condition were first solutionized at 465 ± 2°C for 1 hr. in a salt bath, water-quenched and immediately reaged in a silicone oil bath controlled to ±1°C. The two step T76 treatment consisted of aging the samples for 8 hrs. at 100°C, water quenching, and subsequently aging at a higher temperature, 165°C, for 24 hrs.

Thin foils for electron microscopy were prepared using disks 3mm in dia., which had been punched from the strips and mechanically polished to 0.12mm in thickness. These were first polished using jet electrolytic polishing to form dimples on the center of both faces in a solution of 10% HNO_3, 90% H_2O at 20 Volts at room temperature. This was stopped prior to perforation, and final thinning was performed by conventional polishing at -20°C in an electrolyte of 30% HNO_3, 70% CH_3OH at 15 Volts. Some of the dimpled samples were finally polished using an ion milling machine to avoid a slight oxidation problem encountered during electrolytic polishing. The applied potential during ion milling was 4.6 KV, using an Ar^+ ion probe current of 25μA from both guns. All the TEM was done at 100 KeV using JEOL 100 CX TEMSCAN equipped with a side-entry goniometric double tilting stage.

III. Results

III-1 Retrogression and Reaging Curves

The results of the Knoop hardness measurements are shown in Fig. 1 as a function of immersion time at the retrogression temperature, 240°C, before and after reaging at 120°C; the closed circles represent the retrogression curve, while the open circles indicate the retrogression and reaging curve. Each point represents the mean value of measurements on five disks. The retrogression curve shows that the microhardness initially decreases with immersion time, reaches a minimum at about 25 s and then increases up to about 40 s before decreasing again. The measurements on the samples subjected to the retrogression and reaging treatment indicate that up to about 30s the retrogressed specimens recover more than 95% of their original T651 hardness after reaging. After 30s, the microhardness decreases with immersion time. To determine the retrogression time at 240°C, the time interval necessary for the strips to reach the retrogression temperature was measured using a strip sample in the form of an intrinsic thermocouple. Two wires of a thermocouple were spot-welded (the distance between the two wires was 3mm) to a stainless steel strip of the same thickness as the Aℓ 7075 strips. The temperature was monitored as a function of immersion time, as illustrated in Fig. 2. The result shows that about 10 to 15s is required for the strips to reach 240°C. Assuming similar thermal behavior of stainless steel to that of the Aℓ 7075 alloy, it is estimated that 10 to 15s is the optimum retrogression time. However, since the thermal conductivity of 7075 is greater (approximately 9 times), than that of stainless steel, the actual optimum time is expected to be shorter than that.

The fractional standard deviation of the hardness values in Fig. 1 was about 11% for the retrogression and reaging curve and about 13% for the retrogression curve, indicating that the measured values are somewhat scattered. The depth of the microindentation was calculated in order to examine the possible influence of the thickness of the strips on the results. The calculation indicated that the maximum indentation depth, corresponding to the measured indentation length, is about 5μm. This indicates that strips thicker than 50μm are safe enough for the measurements. Since the thickness of the strips studied was greater than 100μm, it appears that the error does not arise from the small thickness of specimens. It may probably arise from the strong directional grain orientation of the ST-L section and local variations in the smoothness of the surfaces of the specimens.

III-2. Transmission Electron Microscopy

Typical bright field images of samples in 3 different heat treatment conditions, T651 as-received, T76 and RRA are illustrated in Fig. 3; the RRA microstructure is represented by the sample retrogressed for 30s immersion time (RRA-30). Figure 3 also presents a typical example of a bright-field image of the retrogressed condition for 30s immersion time without the subsequent reaging-treatment (R-30). The particles are generally plate-shaped, although there are some small spherically shaped particles, particularly in the T651 and RRA conditions. Their sizes are generally small in the T651 and coarse in the T76 conditions. The particle sizes in RRA-30 appear to be intermediate between those in the T651 and T76 conditions. The particle density appear to be high in both the T651 and RRA-30 conditions, but substantially lower in the T76 case. The characteristic feature of the R-30 microstructure is a significantly lower particle density as compared with that of the RRA-30 condition. Some of the particles, particularly the finer plate-shaped ones, exhibit a line of no contrast in their elongated direction which is parallel to [110] and perpendicular to the direction of the diffraction vector $\vec{g} = (1\bar{1}1)$ in a foil orientation near $[\bar{1}12]$. Such contrast suggests that the precipitates are coherent[71] on {111} planes. This is further supported by the observation of the strain field associated with precipitates, which produces an image size that is greater in the bright-field than in the dark-field image.

III-2.1 Identification of Precipitates

Figure 4 shows respectively, the selected area diffraction patterns of thin foils with zone axes of the type $B = \langle\bar{1}12\rangle$ corresponding to the bright-field images of Fig. 3 for each heat-treatment condition (T651, T76, RRA-30 and R-30). These diffraction patterns appear to be complex due to the simultaneous presence of several precipitates. While the general pattern for RRA-30 appears

to be similar to that for T651, the main difference between the two cases is in the relative intensity of the reflections arising from the precipitates. In both cases relatively intense spots appear at 1/3 and 2/3 (220), near 1/3 $(\bar{1}1\bar{1})$, 1/3 and 2/3 (220). In the T651 case, continuous streaking parallel to $[\bar{1}1\bar{1}]_{A\ell}$ at 1/3 and 2/3 $(220)_{A\ell}$ characterizes the pattern. Close examination reveals that these streaks are usually associated with somewhat intense spots near every 1/6 $(\bar{1}1\bar{1})$, 1/3 (220) and 2/3 (220) position. Relatively intense spots also appear just inside the 2/3 (220), $(\bar{2}2\bar{2})$, and $(\bar{1}1\bar{1})$, 1/3 (220). Two spots near 1/2 $(\bar{1}1\bar{1})$, symmetrically placed on either side of it, are usually present, but their intensity is weak. Although streaking is still present in the RRA-30 samples (Fig. 4), there are generally more discrete spots at every 1/6 $(\bar{1}1\bar{1})$, 1/3 and 2/3 (220), resulting in a cross-grating pattern of rectangular shape consisting of two perpendicular axes parallel to $[\bar{1}1\bar{1}]$ and [220]. Another characteristic feature of the RRA-30 condition is that two spots near 1/2 $(\bar{1}1\bar{1})$, symmetrically placed on either side of it, become intense. Also, the intensity of the spots just inside the $(\bar{2}2\bar{2})$ and $(\bar{1}1\bar{1})$, 1/3 (220) positions usually increases.

The cross-grating pattern associated with the extensive streaking, particularly in T651, can be best indexed as a hexagonal unit cell with $d_{10\bar{1}0} = 3d_{220\ A\ell}$; $d_{0001} = 6d_{\bar{1}1\bar{1}A\ell}$. Considering that this pattern is different from the expected reflection pattern of the various η phases, it is believed that it arises from the transition phase, η', having the morphology of small spherical or plate-shaped particles. Using known values of the lattice parameter of the α solid solution, a = 4.049 Å, the lattice parameters of the η' phase can be calculated as a = 4.96 Å and c = 14.03Å. Its orientation relationship with the matrix is $(10.0)_{\eta'} || (110)_{A\ell}$; $(00.1)_{\eta'} ||$

$(\bar{1}1\bar{1})_{A\ell}$. This orientation relationship of the η' phase with matrix is consistent with that proposed by Gjønnes and Simensen[10]. However, the structure is quite different from the one they have proposed. This result also differs from that of Mondolfo et al.[1] in its value of c. However, it is close to the structure derived from the x-ray results of Auld et al.[17] and is consistent with that derived from the x-ray result of Graf[5] on a pure Aℓ-9Zn-1Mg alloy.

The other spots are believed to arise from the simultaneous presence of the various types of η phase. To index these spots, the technique used by Gjønnes and Simensen[10] and DeArdo and Simensen[13] was applied. When the orientations of the expected precipitates are known, it is possible to construct the positions of their reflections for a given matrix zone axis from the stereographic projections by mapping the possible variants of their orientation relationships. The constructed pattern is then compared with the experimental one to predict the presence of each type of precipitate. Figure 5 shows the schematic diffraction pattern diagram constructed in this way, including the strong spots expected from the η_1, η_2 and η_4 variants. Figure 5 also includes the spots arising from the transition η' phase. Only 3 types from among the 9 variants of the η phase are considered, because those three types are known to be the most frequently observed [10,11] in pure Aℓ-Zn-Mg alloys. This diagram matches quite well with the observed diffraction patterns (Figs. 4a and c), although the observed patterns contain additional spots. It clearly shows that the appearance of the intense spots at 1/3 and 2/3 (220) is due to the superposition of the $(00.2)_{\eta_1}$, $(10.0)_{\eta_2}$, $(00.2)_{\eta_4}$ and $(10.0)_{\eta'}$ reflections. The spot near 1/3 $(\bar{1}1\bar{1})$, 2/3 (220) becomes intense as a result of the superposition of the $(20.2)_{\eta'}$ and $(02.2)_{\eta_1}$ reflections. The reflection $(\bar{1}2.0)_{\eta_1}$ explains the appearance of

the spot just inside 2/3 (220). The appearance of the intense spots near $(\bar{2}2\bar{2})_{A\ell}$ and $(\bar{1}1\bar{1})_{A\ell}$, 1/3 $(220)_{A\ell}$ arises from the superposition of the $(\bar{2}4.0)_{\eta_4}$ and $(00.8)_{\eta'}$ reflections and of the $(10.5)_{\eta'}$ and $(\bar{1}2.2)_{\eta_4}$ reflections, respectively. The appearance of 2 spots near 1/2 $(\bar{1}1\bar{1})_{A\ell}$, symmetrically placed on either side of it, is due to the $(00.2)_{\eta_2}$ reflection and double diffraction on $(\bar{1}1\bar{1})$.

Other thin foils were tilted to other zone axes B = [011] and [001]. Figure 6 presents typical examples of the diffraction patterns for B = [011] and B = [001] of samples in the T651 and T76 conditions, and B = [011] of samples in the RRA-30 and R-30 conditions. The results of the analysis of the reflections in these orientations are quite consistent with the previous analysis for B = $[\bar{1}12]$. For B = [011] in the T651 condition extensive streaking along the two <111> directions, accompanied by somewhat intense spots at every 1/3 {111} positions, is clearly visible (Fig. 6). In the RRA-30 condition, the streaks are manifested as more discrete spots at every 1/3 {111}, confirming the presence of the η' transition phase. The η' spots also appear at 1/3 and 2/3 $(220)_{A\ell}$ in all three orientations studied. The η_1 variant results in the appearance of a $\{\bar{1}2.0\}$ spot just inside 2/3 (220). Also the $(00.2)_{\eta_1}$ spot appears at 1/3 and 2/3 $(220)_{A\ell}$ superposed on the η' spot. The presence of the η_1 phase is further manifested by the $(10.0)_{\eta'}$ reflection near 1/2 (200). This spot appears in samples aged to the T76 condition and in samples heat-treated RRA-60 for B = [011].

The evidence for the η_2 variant is the presence of the $(00.2)_{\eta_2}$ spot near 1/2 $\{111\}_{A\ell}$ for foils with either B = [112] and B = [011]. This spot is usually accompanied by its double diffraction spot on {111}. Along [220], the $(10.0)_{\eta_2}$ reflection appears just inside 1/3 (220) in all three orientations. As evidence of the presence of the η_4 variant, the $(\bar{2}4.0)_{\eta_4}$ reflection appears

just inside $\{222\}_{A\ell}$ for B = [112] and B = [011]. The $(\bar{1}2.2)_{\eta_4}$ reflection appears just inside $(\bar{1}1\bar{1})_{A\ell}$, 1/3 $(220)_{A\ell}$ in the B = [$\bar{1}$12] orientation. The $(00.2)_{\eta_4}$ reflection also appears at 1/3 and 2/3 $(220)_{A\ell}$, superposing on the $(10.0)_{\eta_1}$ and $(00.2)_{\eta_1}$ reflections in all three orientations. Figure 7 summarizes the above discussion, shows schematically the strong spots frequently observed along <220> and <200>, and their expected double diffraction spots, for B = [001]. The same rules can be applied for B = [011].

Although the foregoing analysis can explain the main features of the observed diffraction patterns in all three orientations, there appear to be extra spots in the observed diffraction patterns. Three factors can be considered as the main reasons for the appearance of the extra spots. The first is the effect of double diffraction on the $(111)_{A\ell}$ and $(220)_{A\ell}$ spots. As an example, the spot pattern around the transmitted beam is similar to those around the (111) and (220) spots. Another example is the appearance of two spots near 1/2 $(111)_{A\ell}$ symmetrically placed on either side of it. This is the $(00.2)_{\eta_2}$ reflection with its double diffraction spot on $(111)_{A\ell}$, the exact location of which is $r\ (00.2)_{\eta_2} = 0.54\ r\ (111)_{A\ell}$. Extra spots can also appear due to the presence of other variants in small quantities, T phases, particularly in samples in the T76 and RRA conditions, and other second phases such as Cr-rich precipitates. The presence of the cubic T phase was occasionally observed in this study in samples in the T76 condition.

The other source for extra spots is the presence of γ-$A\ell_2O_3$ oxide films on the thin foils. Such oxide spots appear usually at the intersection of several ring patterns of strongly reflecting planes of polycrystalline γ-$A\ell_2O_3$, such as {400}, {440}, {220} and {311}, due to the occurrence of

multiple double diffraction on several matrix spots, for example {111}, {220} and {311}. This occurs so extensively, particularly for B = [011] that the B = [011] diffraction pattern can show satellites of oxide spots near every matrix spot (Fig. 6). Figure 8 shows schematically how such oxide spots can form through the intersection of multiple ring patterns of polycrystalline γ-$A\ell_2O_3$ films for the three different orientations studied. On comparison of Fig. 6 with the corresponding diffraction patterns in Fig. 8, it is clear that such oxide spots explain many of the strong extra reflections frequently observed. The ring patterns themselves were sometimes observed.

It is believed that the oxides originate from the electrolytic polishing process. Some of the samples in the T651 condition were polished using the ion milling machine to test this conjecture. Figure 9 presents typical examples of the selected area diffraction patterns of two different zone axes B = [112] and B = [011], taken on the foils prepared by ion milling. Compared with Figs. 4 and 9, it is clearly demonstrated that extra spots in Fig. 8 in fact arise from the influence of oxide films. It is interesting to remark that oxide spots at the center of the rectangle defined by $(\bar{1}1\bar{1})$ and [220] for B = $[\bar{1}12]$ still sppear even in the foils prepared by ion milling although their intensity is much reduced. This seems to suggest that the oxide forms rapidly (at least a very thin layer) on the freshly prepared surfaces and probably grows in the TEM.

On the basis of the above analysis of the diffraction patterns, the microstructural features characteristic of each tempering condition can be estimated. The streaking due to the η' phase associated with the T651 condition produces more distinctive η' spots at every 1/6 (111), 1/3 (220) for B = $[\bar{1}12]$ in samples treated to the RRA-30 condition, resulting in the cross-grating pattern. This is interrupted as due to the fact that much of

the η' phase in the T651 condition still remains in a state close to the ordered hexagonal zones described by Graf[3], Schmalfried and Gerold[6] and Lyman and Vander Sande[19]. In the RRA-30 condition, however, much of η' phase transforms to the hexagonal structure. The occurrence of slight coarsening of η' particles due to the RRA-30 treatment, as compared to those in T651 may also contribute to this effect. The $(00.2)_{\eta_2}$ spot near 1/2 $(111)_{A\ell}$ in RRA-30 becomes very distinctive, compared with that in T651. The intensity of the $(\bar{1}2.0)_{\eta_4}$ reflection increases as well. The intensity of all spots along <220>, such as the $(40.0)_{\eta'}$+ $(00.4)_{\eta_1}$ + $(00.4)_{\eta_4}$, $(\bar{1}2.0)_{\eta_1}$, and $(40.0)_{\eta_2}$ reflections also increases, which results in the appearance of a group of four spots near 2/3 $(220)_{A\ell}$ (Fig. 7), the results indicate that the intensity of the reflections reponsible for the η variants, particularly η_2 and η_4, increases as a result of the RRA heat-treatment of the T651 microstructure. Meanwhile, the intensities of the reflections arising from the η variants in R-30 samples are generally similar to those in RRA-30. However, the reflections of the η' phase are usually less intense in R-30, producing streaking along <111> rather than distinctive η' spots.

Significantly different from that of both the T651 and RRA-30 tempers, the diffraction pattern of samples in the T76 temper shows very intense reflections of the η variants. The streaking and cross-grating pattern due to the η' phase are nearly absent. Multiple spots appear near 2/3 $(220)_{A\ell}$ along <220> . Although this basically consists of $(00.4)_{\eta_1}$ + $(00.4)_{\eta_4}$, $(\bar{1}2.0)_{\eta_1}$ and $(40.0)_{\eta_2}$ reflections, similar to those in RRA-30, other spots appear near 2/3 $(220)_{A\ell}$ on either side of it along <111> directions (Fig. 4b, 6b). These spots may arise from other variants of the η phase such as η_5, η_6 and η_7. These three types have the same orientation, $(\bar{1}2.0)_{\eta}$ || $(1\bar{1}\bar{1})_{A\ell}$ as the η_4 type but their $(00.1)_{\eta}$ are slightly rotated around [110]

instead of lying parallel to $(110)_{A\ell}$, as is the case for the η_4 variant [11]. The diffraction pattern B = [112] frequently shows a spotted ring pattern around the transmitted beam (see Fig. 4b), including unidentified extra spots. Similar effects for B = [112] have been reported by DeArdo and Simensen[13] in the overaged pure Aℓ-Zn-Mg alloy. They attributed it to the possible appearance of each η variant of all the η types (there are at least 6 variants of the orientation relationship and 9 different orientation relationships of the η phase). As pointed out previously, the T phase, $(A\ell Zn)_{49}\ Mg_{32}$ observed in the T76 case, can also contribute to the appearance of the extra spots. Generally, the evidence for η' is not extensive in this case, but spots at 1/6 (111), 2/3 (220) usually appear, suggesting that the η' phase is still present in this microstructure. Another point is the appearance of the $(10.0)_{\eta_1}$ reflection near 1/2 $(200)_{A\ell}$ in B = [011]. This spot is usually accompanied by steaking along <100>, indicating the presence of fine η_1,type particles on (100) planes as a result of the two-stage heat treatment (Fig. 6b).

The diffraction patterns from samples in the RRA-10 and RRA-60 conditions have also been studied. Figure 10 presents typical diffraction patterns for B = [112] and B = [011]. The diffraction patterns for the RRA-10 condition appear to be similar to those for T651, in general. However, the reflections responsible for the η phase, particularly η_2, appear to be somewhat more intense than those for T651 and the streaking along <111> tends to contain more discrete spots due to the η' phase. The diffraction patterns for the RRA-60 condition are rather similar to those for T76 with regard to the reflections arising from each type of η variant. However, even in the RRA-60 condition η' spots are visible, sometimes accompanying the streaking, although the extent of the streaking is comparatively small.

III-2.2 Characterization of the Microstructures of the T651, T76 and RRA Tempers

The results of dark-field image study confirmed the information obtained from the analysis of the diffraction patterns. The reflections responsible for each type of precipitate are generally closely related to each other, as seen in Figs. 4 and 6. This makes it difficult to separate the reflections due to each precipitate, since more than 2 reflections arising from different precipitates can easily enter an objective aperture of even the smallest size. Nevertheless, it is possible to assess the shape, size, and quantity, etc., of each type of precipitate by taking dark-field images using characteristic reflections associated with each type which can be separable from other spots and by taking a series of dark-field images using various strong spots including reflections arising from more than two types and comparing them. For example, the η_1 and η_2 variants can usually be isolated using their $(\bar{1}2.0)_{\eta_1}$ and $(00.2)_{\eta_2}$ reflections respectively. The η' phase can be distinguished from the others by using the $(00.2)_{\eta'}$ reflection. The η_1 and η_2 types and η' phase can be also distinguished by comparing dark-field images taken using 2/3 (220), ~ 1/3 $(\bar{1}1\bar{1})$, which includes $(20.2)_{\eta'}$, $(02.2)_{\eta_1}$ and $(20.1)_{\eta_2}$, dark-field images taken using 1/3 (220), 5/6 $(\bar{1}1\bar{1})$which includes $(10.5)_{\eta'}$, $(10.3)_{\eta_2}$ and $(\bar{1}2.2)_{\eta_4}$ and dark-field images obtained using the $(\bar{1}2.0)_{\eta_1}$ + $(20.0)_{\eta_2}$ reflections. The η_4 variant is usually recognizable by its particular lath type morphology, although they usually appear simultaneously with the other types due to the close proximity of their reflections to those of the others. The most intense spot at 2/3 $(220)_{Al}$ includes the reflections of all four types, i.e., $(20.0)_{\eta'}$, $(00.4)_{\eta_1}$, $(20.0)_{\eta_2}$ and $(00.4)_{\eta_4}$.

The results of the studies on the morphology of the precipitates, mainly the examination of various dark-field and bright-field images of thin foils in various orientations, lead to the conclusion that the η' particles are either

spherically shaped or plate shaped, while the η_1 and η_2 types are plate-shaped and the η_4 type is usually lath shaped, confirming previous results on pure Aℓ-Zn-Mg alloys [10,11].

Figures 11a and 11b are, respectively, dark-field images of the RRA-30 condition, taken using the $(20.0)_{\eta'}$ + $(\bar{1}2.0)_{\eta_4}$ and $(\bar{1}2.0)_{\eta_1}$ reflections in B = [011]. The many fine precipitates in Fig. 11a are mostly η' particles of spherical or plate shape, which are extended in the direction perpendicular to [111], indicating that the η' lies on (111). Figure 11b shows many η_1 plates which are extended in the direction perpendicular to [220], suggesting that they are on (110). Figures 11c, 11d, 11e and 11f show another example of dark-field images from an RRA-30 sample, taken using various reflections in B = [112]. Figure 11c, taken using 2/3 (220), which includes $(20.0)_{\eta'}$ + $(00.4)_{\eta_1}$ + $(20.0)_{\eta_2}$ + $(00.4)_{\eta_4}$, shows all four types of precipitates. Figure 11d shows the dark-field image taken using $(20.4)_{\eta'}$, though this spot usually includes $(02.2)_{\eta_1}$ and $(20.1)_{\eta_2}$ due to their proximity. It demonstrates the presence of many fine η' particles of spherical or plate shape, and some rather coarser η_2 plates on $(1\bar{1}1)$ extending along [220], and some fine η_1 plates lying on (110). Some fine η_1 plates lying on (110) are clearly shown in Fig. 11e, which is taken using $(\bar{1}2.0)_{\eta_1}$. Some coarse lath-type particles η_4 lying on $(1\bar{1}1)$ are also seen in Fig. 11e. This is probably due to the presence of the $(00.4)_{\eta_4}$ reflection in the objective aperture. The lath type η_4 is best seen in Fig. 11f, taken using the $(\bar{1}2.2)_{\eta_4}$ + $(10.5)_{\eta'}$ reflections.

Typical examples of dark-field images from samples in the T651 condition are presented in Fig. 12, which were taken from a thin foil with B = $[\bar{1}12]$. Many fine η' phase particles of spherical or plate-shape, lying on $(1\bar{1}1)$, are seen in Fig. 12a, which is taken using 1/3 $(220)_{A\ell}$, 5/6 $(\bar{1}1\bar{1})_{A\ell}$, including the $(10.5)_{\eta'}$ spot associated with streaking. The dark-field image of Fig. 12b, which was taken using 2/3 $(220)_{A\ell}$ including $(20.0)_{\eta'}$

associated with streaking and $(00.4)_{\eta_1} + (20.0)_{\eta_2} + (00.4)_{\eta_4}$, also shows many η' particles. The dark-field images taken using η' reflections associated with streaking usually present both the spherical and plate-shaped particles. Their sizes are usually small; the diameter of the plate-shaped particles is about 50 to 60Å and the size of the spherically-shaped particles is generally smaller than 50Å, ranging from 30 to 50Å. Because of the small size of the apparently spherical particles, it is sometimes not clear if they actually have a spherical shape or are instead small plate-shape precipitates. When tilting the beam slightly from the exact η' position along a streak, both the spherical and plate-shaped particles disappear. This is taken as evidence that the fine spherically-shaped particles (Figs. 12a and 12b) have the same hexagonal structure as the fine plate-shaped particles. This conclusion is similar to that made on the η' of spherical shape that appear during the early stages of aging of pure Aℓ-Zn-Mg alloys[10].

It was previously illustrated in Fig. 3a that many fine particles show evidence of coherency strains, exhibiting a line of no contrast on the {111} planes. Comparison of Fig. 3a with Fig. 12a indicates that most of these particles are η' particles, suggesting that η' particles are usually coherent with the matrix. Figure 12c, taken using the $(01.1)_{\eta_1}$ reflection, shows the plate-shaped η_1 variant. Figure 12d, taken using the $(00.1)_{\eta_1}$ reflection, shows the plate shaped η_1 variant. Figure 12d, taken using the $(00.2)_{\eta_2}$ reflection, shows a few η_2 plates lying on the same plane as the η' particles. Detailed analysis of the various dark-field images indicates that the fine η' particles of spherical or plate shape are the predominant phase in the T651 temper. However, some η_1 particles are also present in appreciable quantity, together with η_2 particles in small quantity. The η_4 variant is rarely observed in this case. The sizes of the η precipitates, as well as the η' particles, are generally small compared with those in the RRA-30 condition.

On the other hand, the RRA-30 microstructure contains relatively many η particles, particularly the η_2 and η_4 types. The sizes as well as the quantities of the η_1, η_2 and η_4 types increase substantially during the RRA treatment by comparison with T651 temper (cf. Figs. 11 and 12). However, it is interesting to note that the microstructure of RRA-30 still contains many relatively fine η' particles of spherical or plate-shape (Fig. 11) frequently exhibiting coherency contrast, and that the overall particle density in RRA-30 microstructure is comparable to that of the T651 condition (Fig. 17, Table 1).

It is interesting to remark that some of the fine η' particles frequently have a linear appearance in the RRA-30 condition (Figs. 11a and 11c). These are also observed sometimes in the T651 microstructure (Fig. 12c). Their lengths are sometimes long ($\sim$ 100 to $\sim$ 150 Å), while their widths are usually small, being less than 20 Å. These features sometimes appear to have degenerated into individual particles of both the spherical and plate shape, along certain directions as shown in Fig. 11g, which was taken using the (00.4) η' + $(\bar{1}2.0)$ η_4 reflections (the region of the foil is identical to that in Fig. 11h). These become visible only in dark-field images taken using η' reflections. To test the possibility that such dark-field images arise either from drift due to long exposure times or spherical observation due to slight misalignment, these images should be carefully compared to their bright field images (cf. Figs. 11g and 11h). The result reveals that such features are effectively present in the bright-field image, although careful scrutiny is required to recognize them due to their faint contrast. The careful analysis of many dark-field images formed using η' reflections, and their companion bright-field images, leads to the conclusion that the origin of the streak-like features is fine η' particles nucleated on dislocation cores.

The dark-field image in Fig. 12e well illustrates this conclusion; it was taken using the (00.8) η' reflection from the same region of the foil as the bright-field image in Fig. 12f. It is seen that the fine linear features resulting from the image of the η' reflection appear along the dislocation lines. Sometimes they appear to have degenerated into discrete particles of both spherical and plate-shape. This suggests that some of the fine η' particles nucleate heterogeneously on dislocations in both the RRA-30 and T651 conditions. This was observed more frequently in RRA samples than in T651 samples. It is easily understandable in T651 samples, since the introduction of new dislocations by stretching after solution-treatment provides more sites for heterogeneous nucleation.

Typical examples of dark-field images of samples in the T76 temper are seen in Fig. 13. They were taken using 2/3 (220), which includes (20.0) η' + (00.4) η_1 + (20.0) η_2 + (00.4) η_4, $(\bar{1}2.0)\eta_1$ + $(20.0)\eta_2$, $(\bar{1}2.0)\eta_4$ and $(10.5)\eta'$ + $(10.3)\eta_2$ + $(\bar{1}2.2)\eta_4$, respectively, in thin foils with B = $[\bar{1}12]$ in similar areas to that seen in Fig. 3b. The absence of significant differences between the features seen in Figs. 13a and 13b indicate that the η_1 and η_2 variants constitute the principal precipitates in this case. Some edge-on η_4 laths are visible in Fig. 13c. Figure 13d shows some η_2 and η_4 lying on $(1\bar{1}1)$; the quantity of the η' particles is significantly reduced, confirming the analysis of the diffraction patterns. On comparison of Fig. 13 with Figs. 11 and 12, it is evident that the sizes of the η particles are in general much coarser than those in T651 samples and also those in RRA-30 samples (Table 1 and Fig. 17). However, the sizes of some of them, particularly the η_1, variant are small, ranging from 50 to 100 Å. This is probably due to the two step heat treatment effect[7,16] and explains the appearance of the $(10.0)\eta_1$ reflection, which is sometimes associated with streaking parallel to <100>. It is also worth remarking that precipitates formed on dislocation lines are hardly observed in this case.

Figure 14 presents some typical examples of dark-field images of samples in the R-30 condition. The dark-field image of Fig. 14a was obtained using the reflection at 1/3 $(\bar{1}11)$ in a foil oriented B = $[0\bar{1}1]$. The operating precipitate reflection is $(00.2)_{\eta'}$, but this is probably interfered with by $(00.2)_{\eta_2}$ and $(\bar{1}2.0)_{\eta_4}$ due to the usual strong double-diffraction effect in this zone axis. The reflection $(20.2)_{\eta'}$ + $(20.1)_{\eta_2}$ + $(02.2)_{\eta_1}$ was used to take Fig. 14b in which B = $[\bar{1}12]$. Figure 14a presents very fine η' particles of spherical and plate-shape, together with generally coarse η_2 and η_4 on $(\bar{1}11)$. Fig. 14b shows some very fine η' particles of mostly spherical shape and coarse η_2 plates on $(1\bar{1}1)$. Some η_1 on (110) is also faintly seen. Comparing the dark-field images of R-30 samples with those of RRA-30 samples (Fig. 11), one can notice three interesting features. The first consists of the apparently significant reduction in the overall particle density in the R-30 sample. Measurement shows that the number of particles per unit area, N is approximately 1/3 of that in RRA-30 samples. The second point is that the quantities, as well as the sizes of the η particles, particularly the η_2 and η_4 types, are very similar to those in RRA-30 samples (Table 1 and Fig. 17). Measurements indicate that the fractional quantities of each η variant in the R-30 microstructure increase to about 3 times those in the RRA-30 structure. Finally, the quantity of η' particles appears to be significantly reduced. Their sizes are smaller than even those in the T651 temper, and particles with spherical morphology are more abundant than those with plate-shapes.

The microstructures of RRA-10 and RRA-60 samples were further studied to evaluate the role of the RRA treatment. Some typical examples of dark-field images of both types are presented in Fig. 15 (RRA-10) and Fig. 16 (RRA-60). Figure 15a, taken using the reflections $(20.0)_{\eta'}$ + $(00.4)_{\eta_1}$ + $(20.0)_{\eta_2}$ + $(00.4)_{\eta_4}$ in B = $[\bar{1}12]$, reveals many fine spherical and plate-shaped precipitates which are mostly η' particles. The dark-field image formed by the $(20.4)_{\eta'}$ +

$(02.2)_{\eta_1}$ + $(20.1)_{\eta_2}$ reflections (Fig. 15b) shows some coarse η_2 plates as well as many fine η' particles on $(1\bar{1}1)$. The η_1 plates are also seen on (220), though faintly, due to the slight deviation of the objective aperture from the exact position of the $(02.2)_{\eta_1}$ reflection. The characteristic features of the RRA-10 microstructure consist of a significant increase in the sizes of the η phase precipitates, compared with those in T651 samples, without considerable differences in the quantity and size of the η' particles. Also, the quantity of η phase precipitates, particularly the η_2 type, is increased (Table 1, Figure 17). Figures 16a, b and c were taken using the $(20.0)_{\eta'}$ + $(00.4)_{\eta_1}$ + $(20.0)_{\eta_2}$ + $(00.4)_{\eta_4}$, $(\bar{1}2.0)_{\eta_1}$ + $(20.0)_{\eta_2}$ and $(10.5)_{\eta'}$ + $(10.3)_{\eta_2}$ + $(\bar{1}2.2)_{\eta_4}$ reflections, respectively, in B = $[\bar{1}12]$. In Fig. 16b many coarse η_1 plates, as well as some η_2 plates, are visible. Fine η' phase particles and coarse η phases of the η_2 and η_4 variants are seen in Fig. 16c on $(1\bar{1}1)$. Compared with RRA-30 samples, two points are particularly noteworthy regarding the RRA-60 heat-treatment: The first is that the quantity of the η phase precipitates, particularly the η_1 and η_4 variants, increases significantly. This is consistent with the information obtained in the analysis of diffraction patterns showing, particularly, the appearance of the $(10.0)_{\eta_1}$ reflection for B = [011]. The other is that extensive coarsening of the η particles of all variants occurs (Table 1 and Fig. 17). Their sizes are very comparable to those in T76 samples, but the RRA-60 samples still contain fine η' particles in contrast with T76, frequently along dislocation lines (Fig. 16c). The overall particle density appears to be higher than that in T76 samples.

Table 1 summarizes the results of the studies of the dark-field images: It presents the approximate relative quantities of the η', η_1, η_2 and η_4 particles resulting from each heat-treatment condition investigated, together with their morphology. The particle sizes of each type were measured

exclusively from the dark-field images. At least 100 particles were measured from four dark-field images taken from different regions in the thin foil. The longest dimensions were measured for the plate-shaped particles. The number of particles per projected unit area, N, was measured in the highest density region of the projected area. At least three different dark-field images were analyzed for each heat-treatment condition. Figure 17 presents the overall particle size distribution measured from dark-field images taken using 2/3 $(220)_{A\ell}$, which includes the reflections of all 4 types of precipitates (e.g., Figs. 11c, 12b, 13a, 15a and 16a). Their mean particle sizes are also included in Table 1. For this purpose at least 300 particles were measured from more than three different dark-field images in enlarged prints. Figure 18 illustrates the variation of the overall mean particle diameter, $\bar{d}$ with the retrogression time (immersion time). It also includes the variation of the overall particle density with the immersion time. It is interesting to note from Fig. 18 that no distinctive overall coarsening of the particles can be seen during the initial period (up to 20-30s of immersion time), while the coarsening occurs rapidly afterwards. This happens although significant coarsening of the η phase, particularly the η_1 and η_4 variants, occurs during the initial period.

III - 2.3 Microstructure of Precipitates on Grain Boundaries

The microstructure of the regions near grain boundaries were examined, in an attempt to correlate the PFZ size, precipitate size, etc., to the SCC characteristics of the alloy in each heat-treatment condition. The presence of a PFZ adjacent to grain boundaries is typical of the various RRA conditions, as well as of the T651 and T76 tempers. In the extruded Aℓ 7075-T651 alloy, grains markedly elongated along the extrusion direction were typically observed. The PFZ was commonly found along the long grain boundaries parallel to the extrusion direction: ST-L sections, which are the most susceptible to SCC

contain many long PFZs along elongated grains (Fig. 19a). On the other hand, L-T sections, which are the least susceptible to SCC, contain an equiaxed random grain structure. The PFZ forms along such random grain boundaries, but its occurrence appears to be much less than in ST-L sections (Fig. 19b). Typical examples of PFZs in RRA-30 and T76 samples are shown in Figs. 19c and d, respectively. Evidence for the two-stage heat-treatment sometimes appeared in the PFZ of samples in the T76 temper (i.e., the presence of small particles in the original PFZ). The widths of the PFZ in each case were measured and are presented in Table 2. The PFZ in the T76 temper sometimes appears to be slightly larger than in the other tempers, but no significant differences can be found in general, considering the scatter in their widths. This observation is consistent with that of previous work[28,40,41,48], in which it has been reported that no definite trend can be found between the width of the PFZ and the susceptibility to SCC.

It was not always possible to identify the grain boundary precipitates because of the usual complex diffraction patterns near grain boundaries. However, a suitable orientation may result, in particular cases, in the same diffraction pattern from both of the grains adjacent to the grain boundary. In this situation, the dark-field technique can be applied to identify the types of grain boundary particles. One such example is presented in Fig. 20 for a RRA-30 sample; both grains across the grain boundary have the same orientation, B = [$\bar{1}$12] (Fig. 20b). The dark-field images in Fig. 20c and d were taken using the $(20.0)_{\eta'}$ + $(00.4)_{\eta_1}$ + $(20.0)_{\eta_2}$ + $(00.4)_{\eta_4}$ and $(20.0)_{\eta_2}$ + $(\bar{1}2.0)_{\eta_1}$ reflections, respectively. The precipitates on the grain boundary are clearly shown in Fig. 20c, and still visible in Fig. 20d, indicating that they are the η_1 or η_2 types. The observation of the morphology of the precipitates may be helpful to roughly identify them, because the sizes of the particles on grain boundaries are usually large (order of ~ 400 Å). Both the η_1 and η_2 types are plate-shaped, while the η_4 type usually has a lath shape. T phase has an irregular

morphology. Most of the grain boundary particles appeared to be plate-shaped (Fig. 21), confirming they are mostly η_1 or η_2. The T phase is occasionally observed.

The grain boundary structures were examined by tilting the thin foils through the necessary angles to make the grain boundaries as normal as possible to the electron beam. Figure 21 shows typical examples of the microstructure of G.B. particles in T651, RRA-30, R-30, and T76 samples, respectively. The sizes of the particles in T651 samples are relatively small and the number of particles is high. Distinctively different from those in T651 samples, the sizes of particles are coarse and their number is low in T76 samples. It is interesting to compare the sizes and number of particles in RRA-30 samples with those in T651 and T76 samples. Their sizes are much coarser than those in T651 and comparable to those in T76. Their number is relatively low. The microstructure of grain boundary particles in RRA-10 and RRA-60 samples was further examined to study the role of the RRA treatment. Typical examples of the precipitates on grain boundaries in RRA-10 and RRA-60 are respectively presented in Figs. 21e and f. It is interesting to note in Fig. 21e that the sizes of the particles are already distinctively coarser than those in the T651 temper after the retrogression treatment of only few seconds (immersion time = 10s). On the other hand, the sizes and numbers of particles in RRA-60 samples are not significantly different from those in RRA-30, although the retrogression time is almost doubled.

Measurements of the particle sizes,number of particles per unit area and line fraction, as well as the area fraction of the grain boundary covered by particles,were performed using bright-field images such as those in Fig. 21. The particle sizes were taken to be the longest dimension of the plates along the direction of the grain boundary. More than 100 particles in 5 different grain boundary areas were generally measured in each case. Figure 22 illustrates the

size distribution of the particles measured in this way for samples in the six different heat-treatment conditions. The number of precipitates per unit area, N_A, was measured directly from micrographs with a projected area of ~ 0.15 μm^2. The projected area was used for the area calculation. It was hard to measure the exact tilting angles of the grain boundaries. However, it was estimated that the maximum error arising from the different tilting angles from one sample to another will be less than ~ 13%. Errors may also arise from the projected images of matrix precipitates into the grain boundary. This error is relatively small for samples in the T76, RRA-60 and RRA-30 conditions, since their sizes in general are much coarser than those of the matrix precipitates, as can be verified on comparison of Fig. 22 with Fig. 17. However, this error can be more serious for T651 and RRA-10 samples. Particular caution was taken to distinguish the possible projected matrix particles on grain boundaries by comparing them with particles in the matrix adjacent to the grain boundary. The line fractions covered by particles on the grain boundaries, L_A, were measured using parallel lines drawn on the micrographs parallel to the intersection of the grain boundary and the foil surfaces. The spacing of the parallel lines was 0.01 μm and their length was usually 0.9 μm. Ten lines were usually used in each analysis and more than 5 grain boundaries were examined for this purpose in each case. The area fraction covered by particles , A_A was measured using grids of 0.01 μm interval. The measured areas were usually 0.09 μm^2. Two points can be considered as the major sources of errors in the measurement of L_A and A_A. The first is the problem of overlapping of particles in the projected area. This problem was avoided by choosing proper grain boundary areas. The second is the orientation dependence of the projected particle shape due to the different aspect ratio of particles in each condition.

It was assumed that the aspect ratios of particles in all conditions are the same. The results are summarized in Table 2. Two points are worth noting in Table 2: the first is that the mean particle size, $\bar{d}$, and the line fraction, L_A, in RRA-30 samples are significantly larger than those in T651 samples and comparable to those in T76 samples. The value of N_A is also small in RRA-30 samples, similar to that in T76 samples. However, the size distributions of the grain boundary precipitates in RRA-30 as well as the other RRA samples appear to be broader than those resulting from the T651 and T76 tempers. Some of the grain boundaries contain relatively small particles, comparable to those in the T651 samples. This results in a bimodal distribution of particle sizes in all RRA samples, which is reflected in Fig. 22. The other point is that the mean particle size, $\bar{d}$, as well as N_A in R-30 samples,are very similar to those in RRA-30 samples. The distribution of particle sizes is similar as well (Fig. 22). Figure 23, which summarizes the results of the effect of RRA treatment on G.B. particles, illustrates the variation of $\bar{d}$, L_A, and N_A as a function of the immersion time. It also includes the values resulting from the T76 temper for the purpose of comparison.

IV. Discussion

The results of the microstructural studies indicate that there are no apparent differences in the type of precipitates in the three different temper conditions T651, T76 and RRA. The characteristic feature of the T651 microstructure consists of the predominant presence of fine coherent η' particles of mainly plate shape, about 50 Å in dia. on {111} planes. It also contains some η_1 plates on {110} or {100}, as well as a small amount of the η_2 plates on {111} planes (Table 1). The η_4 (lath shape) is rarely observed. The microstructure of the overage (T76) temper mainly consists of relatively coarse η phases, particularly the η_1 and η_2 variants. The quantity of η' particles is generally small. The overall particle density is relatively low compared with that in T651 and RRA-30 samples. Considering that the maximum hardness of Al 7075 is associated with the T651 temper, it is believed that the fine dispersion of the coherent η' plates is mainly responsible for maximum hardness in this alloy. These results differ from those previously reported by Adler and DeIasi[28-30] in their TEM studies, in conjunction with the study of SCC and DSC measurements. They concluded that G.P. zones are the predominant precipitates in the T651 temper and that the T73 temper is mainly associated with the η' transition phase. However, it is not clearly stated in their studies how the G.P. zones and η' phases, as well as the η variants, were identified. Adler and DeIasi reported that the precipitates were identified simply on the basis of observations of their size and morphology. However, as shown in Fig. 17, the sizes of the precipitates are widely distributed. The present results indicate that the sizes of the η' particles vary from 30 Å to 100 Å in T651 samples and even more (to 150 Å) in RRA-30 samples. The variation of the particle sizes of the η_1 and η_2 variants is even larger, usually ranging from ~ 50 to ~175 Å in T651, ~ 50 to ~ 250 Å in RRA-30 and ~ 50 to ~ 400 Å in T76 samples. It appears that there is no critical size range for the existence

of each phase. Concerning the morphology of the precipitates, all the η', η_1 and η_2 particles are plate-shaped. Thackery[11] reported, in his diffraction pattern analysis of individual particles in an overaged pure Aℓ-Zn-Mg alloy, that the η' variant appeared as elongated 8-sided platelets and the η_2 variant had the shape of either hexagonal or rounded platelets. Such slight differences between the shapes of the η_1 and η_2 plates could not be positively recognized in the present studies, probably due to the fact that their sizes were too small for such an estimate. Of the 3 principal variants of the η phase, only η_4 could be distinguished from others in suitable foil orientations by its particular lath-type morphology. Hence, it appears that the observation of the sizes and morphologies of the particles cannot provide any positive identification method of the precipitates, at least in the case of Aℓ 7075.

The present results on the microstructures of T651 and T76 samples appear to be consistent with the results of previous studies on pure Aℓ-Zn-Mg alloys[10,13,14,24,25]. Kelly and Nicholson[25], Nicholson et al.[24] and Gjønnes and Simensen[10] have reported that the microstructure of pure Aℓ-Zn-Mg alloys at peak hardness consists mainly of η' plates. Meanwhile, Thomas and Nutting[14] and DeArdo and Simensen[13] concluded that the degree of dispersion of both the η' and η phases is a more important factor in the strengthening than the type of precipitate. DeArdo and Simensen[13] have studied two-step aging of the pure Aℓ-7Zn-2.3 Mg alloy, subjected to preaging at 100°C and subsequent final aging at 180°C; this is similar to the heat-treatment conditions of the T76 temper. They found that the overaged microstructure of the Aℓ-7Zn-2.3Mg alloy contains mainly η_1 and η_2 variants.

So far neither the equilibrium phase diagram nor the non-equilibrium constitution diagram of the Aℓ-Zn-Mg ternary system near the retrogression temperature of 240°C are available. Furthermore, the effect of minor alloying

elements, such as ~ 1.6 Cu and ~ 0.23 Cr, which the commercial Aℓ 7075 alloy contains, on the constitution diagrams is unknown. Referring to the known Aℓ-Zn-Mg ternary equilibrium and non-equilibrium constitution diagram at 177°C as a reference[72], one can notice that even after the long aging time of 1 week at 177°C, an Aℓ-Zn-Mg alloy of similar composition to Aℓ 7075 is still in a transition state (in the α + T' + η region), far from the equilibrium state of $\alpha + Mg_3Zn_3A\ell_2$. This example indicates that the retrogression treatment of such a short duration as 10 to 15s at 240°C would lead to a more complex transition situation. Nevertheless, some important effects of the RRA treatment on the T6 microstructure can be deduced from the present results.

Although the processes occurring during the retrogression treatment appear to be complex, they can be summarized in four principal points: Firstly, comparing the RRA-30 and R-30 structure leads to the conclusion that the dissolution of small particles, particularly η', occurs, due to the Gibbs-Thompson effect[73]. Results indicate that a significant fraction, ~ 1/3 of the total particles, dissolves. The true dissolved fraction of the total particles is expected to be even greater, since the R-30 structure probably includes fine η' particles arising from natural aging. It is known that 7075 alloy tends to be continuously aged at room temperature[72]. This natural aging may explain the presence of very fine η' particles, particularly the spherically shaped ones observed in R-30 samples. Secondly, the coarsening of particles occurs; comparing the structures of RRA-30 and T651 tempers indicates that the RRA treatment causes a significant increase in the sizes of the η particles, particularly the η_1 and η_4 variants. This occurs mostly during the retrogression treatment, since the sizes of the η particles in RRA-30 samples are similar to those in R-30 samples (Fig. 17, Table 1). Some of large η' particles appears to grow at the same time, since the mean η' particle size in RRA-30 structure is slightly larger than in T651 structure. The RRA-10

structure indicates that some coarsening of η particles has already occurred after a few seconds of retrogression treatment. As the retrogression time increases from 30 to 60 s, distinctive coarsening of all η variants occurs. Thirdly, the phase transformation appears to occur during the retrogression treatment from the early stages. The results show that the number of η particles, particularly η_2 in the RRA-30 structure, significantly increases, while the number of η' particles decreases, compared to the T651 structure. The number of η_4 particles increases in an appreciable amount as well. The RRA-10 structure shows that the number of η particles, particularly η_2, already increases in an appreciable amount at a very early stage of the retrogression treatment. These results can be interpreted as an indication that some of the stable η' particles transform to η particles, particularly η_2, which have the same orientation relationship with the matrix as the η' phase, i.e., $(10.0)_{\eta'} \parallel (110)_{A\ell}$; $(00.1)_{\eta'} \parallel (\bar{1}1\bar{1})_{A\ell}$. It is also possible that η' particles transform to η_4 variants, since η_4 has the same habit plane, {111}, as the η' phase. This can be explained by the theory of two-step aging of Lorimer and Nicholson[7,15], which proposes that G.P. zones formed during low temperature aging, the sizes of which are larger than the critical size, survive during the up-quench and transform to the η' transition phase. Gjønnes and Simensen[10] and DeArdo and Simensen[13] previously reported in their studies of two step aging of pure Aℓ-Zn-Mg alloys that the η' particles formed at lower aging temperature transform to η_2 particles during up-quenching. Finally, the RRA-60 structure shows that as the retrogression time increases from 30 to 60s, the number of η particles, particularly η_1, increases. The results suggest that this occurs mostly during the retrogression treatment. The reason for this is not well understood. It may be, however, possible that some of the untransformed clusters remaining stable during the retrogression treatment would directly transform to η_1 particles, confirming the theory of two-step aging of Pashley[16]. Gjønnes and

Simensen[10] and DeArdo and Simensen[13] found in pure Aℓ-Zn-Mg alloys that η_1 can be formed directly from stable clusters during aging at relatively high temperatures (150 and 180°C). Thackery[11] found that η_1 forms abundantly during aging of an Aℓ-6Zn-2Mg alloy at temperatures between 135 and 165°C after room temperature quenching. However, a detailed understanding of the complex phase transformations occurring during the retrogression treatment may require information on the temperature dependance of the stability of each phase involved in this process.

The process occurring during the reaging treatment at the temperature of the original T6 temper appears to be mainly the precipitation of the η' phase, since the T651 microstructure mainly consists of η' particles. However, during the reaging treatment the driving force for the nucleation of particles is much lower than it is during the T651 temper. It is possible in this case that heterogeneous nucleation becomes increasingly important in the nucleation process. This probably explains the reason that the fine η' particles are frequently observed along dislocation lines in all RRA conditions investigated. The observation that there is no evidence of precipitation on dislocations during the T76 temper appears to support indirectly this point of view. Although similar observations were made on samples in the T651 condition, the reason for that is probably due to the introduction of plastic deformation before the reaging treatment, as discussed previously.

The retrogression curve of Fig. 1 can now be explained in terms of the results on the RRA microstructure. The initial dissolution of mainly small η' particles, which accompanies significant coarsening of the η phase, is responsible for the initial decrease of hardness. As the retrogression time increases, the additional formation of the η phase, particularly the η_1 variant, occurs, while the existing η phase particles continue to grow, resulting in an increase of the overall particle density. This may explain the slight increase of hardness seen in Fig. 1 following its initial decrease to a

minimum value. Further increasing the retrogression time will lead to the general coarsening of the η phase particles, resulting in a resoftening of the material. The optimum time for the retrogression-treatment is reported[63,66] to be the time corresponding to the minimum hardness in the retrogression curve (Fig. 1). In terms of the present microstructural results, this corresponds to the time at which maximum dissolution of the small η' particles occurs, without appreciable formation of the η phase precipitates. The subsequent reaging treatment will give rise to a reprecipitation of the dissolved solute atoms into many fine η' particles. It is believed that the high strength of the RRA temper, which is comparable to that of the T651 temper is mainly due to the presence of these fine η' particles in the RRA microstructure. The coarsening of the η phase particles, as well as the phase transformations, occurs as well during that time as discussed previously. This probably explains the reason that the RRA microstructure looks like an overaged microstructure, compared to T651, as reported by Lockheed from their optical microscopic observation[66] and by Papazian[31] in his DSC measurements. Papazian reported that the dissolution characteristics of the RRA microstructure were similar to those of the T73 temper. However, the sizes of the η particles (Fig. 17, Table 1) in the RRA-30 samples are still significantly smaller than those resulting from the T76 temper, and relatively small particles ($\sim$75Å in diameter) are predominant in the histogram, while large particles are present, but their proportion is significantly smaller than in the T76 case. Furthermore, the overall particle density in RRA-30 samples is much higher than that in T76 samples (Table 1, Fig. 18), being comparable to that in T651 samples. It is believed that this relatively fine dense distribution of relatively small particles, compared to those in the T76 microstructure, also contributes to the strengthening of the RRA treated Aℓ 7075-T651, confirming previous suggestions[13,14] on pure Aℓ-Zn-Mg alloy.

The results of the studies of the PFZ show that there is no significant difference in their widths among the three different tempers (T651, T76 and RRA), suggesting that the RRA treatment plays no significant role on the width of the PFZ resulting from the original T6 temper. This result is expected, if one refers to the theory of the formation of the PFZ[7,16]. However, it is possible that this treatment could effect the distribution of solute atoms within the PFZ as well as on the grain boundary. The importance of the distribution of solute atoms within the PFZ and the segregation of solute atoms to grain boundaries on the susceptibility to SCC of Aℓ-Zn-Mg alloys have been increasingly emphasized recently by Doig and Edington[49-52], Lorimer et al.[53], Raghavan[54] and Green et al.[55,58].

The results of the study of the microstructure of the G.B. particles indicate that they consist mainly of the η phase variants, particularly η_1 and η_2, in all three temper conditions. It was shown (Fig. 22, 23 and Table 2) that the microstructure of the particles on the grain boundaries is significantly different depending on the heat treatment condition. The microstructure of T651 samples, which is the most susceptible to SCC, consists of a low line fraction covered by particles, L_A, as well as low mean particle size $\bar{d}$, and high particle density, N_A. On the other hand, in the microstructure of the T76 samples L_A and $\bar{d}$ are large, while N_A is small. This is the most resistant microstructure to SCC. The microstructure of the RRA-30 samples contains relatively high values of L_A and $\bar{d}$, comparable to those of T76 samples, and relatively low values of N_A, suggesting that the significant coarsening of the particles on grain boundaries occurs during the RRA treatment. The fact that the microstructure of the R-30 samples is similar to that of the RRA-30 samples suggests that the coarsening of particles on grain boundaries occurs mostly during the retrogression treatment, similarly to what happens to the microstructure of the matrix. The results of the study of the variation of the microstructure of the grain boundary particles with retrogression

time (Fig. 23) illustrate that $\bar{d}$ increases rapidly during the initial period of the retrogression treatment, but the growth rate decreases rapidly as the immersion time increases. It is interesting to note that L_A and $\bar{d}$ vary with immersion time in a very similar manner. N_A decreases rapidly initially (up to ~ 10s of immersion time), but very slowly thereafter. In general, L_A and $\bar{d}$ reach values comparable to those resulting from the T76 temper (to within 90%) in an immersion time of about 30s, although their distributions are broader than in the T76 temper. Both $\bar{d}$ and L_A are already significantly different from those of the T651 temper after only 10s of immersion time. These results differ from the previous result of Papazian[31]. He reported, in his TEM study during the comparative study of the DSC characteristics on T6, RRA, and T73 samples, that the structure of grain boundary particles in RRA samples is similar to that in T6 samples. This is probably because the RRA samples used in his study were bulk samples subjected to the RRA treatment. As pointed out previously, even grain boundary particles in thin samples subjected to the RRA treatment, as in the present study, show a bimodal size distribution.

In general, this initial rapid growth rate characterizes the coarsening process of the particles on the grain boundaries, in contrast with that of the particles in the matrix, where a slow initial growth rate prevails. It does not seem possible to deduce a particular precipitate growth mechanism from the data at such short time intervals (up to 60s). However, it seems quite reasonable to suppose that solute atom diffusion is the controlling step for the growth of the particles in both the matrix[74] and on the grain boundaries[75]. The initial rapid growth rate of the particles on the grain boundaries may be interpreted as due to the fact that it is controlled by grain boundary diffusion, which is much faster than diffusion in the matrix. Since it turns out that dissolution of the small particles occurs at the retrogression temperature,

Ostwald ripening would constitute the main growth process in the matrix. However, on grain boundaries no general dissolution is expected to occur, except for the possibility of the initial dissolution of small particles of the η phase, since most of the particles on the grain boundaries are large η precipitates. This may explain the variation of N_A with immersion time. After its initial rapid drop, no significant change of N_A can be observed. However $\bar{d}$ continues to increase, although its rate becomes increasingly slow as the immersion time increases. These observations seem to suggest that Ostwald ripening will be active only in the early stage of the growth process on grain boundaries.

The recent results of an Auger spectroscopy analysis by Green et al.[52,55] suggest marked segregation of Zn and Mg atoms to grain boundaries in both as-quenched and overaged Aℓ-5.5 Zn-2.5 Mg. It is believed that the segregated solute atoms, if they exist, would also contribute to the coarsening process. The early rapid growth rate of G.B. particles may be partly due to the additive effect of Ostwald ripening and the diffusion of segregated solute atoms to the precipitate during growth. However, further work on the microchemistry near the grain boundaries is needed to test this hypothesis.

On comparing the microstructures of the precipitates on grain boundaries in samples in the T76 and T651 tempers, it is concluded that the susceptibility to SCC of Aℓ 7075 decreases as L_A and $\bar{d}$ increase, and as N_A decreases, which is consistent with previous results on pure Aℓ-Zn-Mg alloys[41-43]. Kent[40,44] also observed in a pure Aℓ-Zn-Mg alloy that the susceptibility to SCC decreases as N_A decreases. Adler et al.[28] reported similarly that the susceptibility to SCC of Aℓ 7075 decreases as N_A decreases. It is believed that the reported beneficial effect of the RRA treatment in Aℓ 7075-T6[63,66],

is due in part to the initial rapid coarsening of G.B. particles, resulting in an increase of L_A and $\bar{d}$ and the decrease of N_A. However, it is not clear which factor is critical to the susceptibility to SCC, the increase of L_A or the decrease of N_A, which results in an increase of the interparticle spacing. Morral and McEvily et al.[41,42] and Peel et al.[43] have emphasized the importance of L_A on the susceptibility to SCC, and have suggested that G.B. particles, acting as sacrificial anodes, are beneficial. On the other hand, others[28,40,44,45] have emphasized the importance of interparticle spacing, suggesting that G.B. particles, giving rise to the crack opening due to the anodic dissolution, are harmful, confirming the earlier point of view of Dix et al.[34,36]. However, the present results on the growth of G.B. particles during the retrogression treatment at 240°C suggest that the coarsening of G.B. particles influences the segregation of solute atoms on the grain boundaries, or the distribution of solute atoms within the PFZ. It is possible that the associated effects of the coarsening of particles greatly contribute to enhancing the SCC resistance of Aℓ 7075. Green et al.[58] have suggested that the segregation of free Mg atoms to grain boundaries may lead to the formation of Mg-H complexes, which would promote hydrogen embrittlement.

V. Conclusions

- The coherent η' phase of both the spherical and plate-shape exhibiting streaking along <111> is identified as having a hexagonal structure of lattice parameter a = 4.96Å, c = 14.03Å. Its orientation relationship with the matrix is $(10.0)_{\eta'} || (110)_{A\ell}$; $(00.1)_{\eta'} || (\bar{1}1\bar{1})_{A\ell}$.

- The microstructures of the commercial Aℓ 7075 alloy in both the peak aged (T651) and the overaged (T76) tempers mainly consist of the η' transition phase of spherical or plate shape and three variants of the η phase: η_1 of plate shape on {110} or {100}, η_2 of plate shape on {111} and η_4 of lath type on {111} planes. The relative quantities and sizes of each phase are different: the microstructure in the T651 temper is characterized by the predominant presence of the fine η' particles with some η_1 plates. The overall particle density is high. The maximum hardness of the T651 temper is believed to arise from the presence of many fine coherent, mostly plate-shaped η' particles. The η' particles sometimes nucleate heterogeneously. The microstructure of the T76 temper consists mainly of relatively coarse η precipitates, particularly the η_1 and η_2 variants. The overall particle density is low.

- The microstructure in the RRA temper consists of two main features: many fine η' particles of spherical or plate shape and somewhat coarse η phase particles. Compared with the T651 temper, the sizes of the η phase particles are coarser and the numbers, particularly of the η_2 and η_4 variants are greater, while many fine η' particles are still present in the RRA condition. Compared with the T76 microstructure, the sizes as well as the quantities of the η particles are still small. The overall particle density is relatively high. The precipitation of fine η' particles occurs frequently by heterogeneous nucleation.

- The precipitates on grain boundaries are mostly η variants in all heat treatment conditions. The T phase is occasionally observed. The susceptibility of Aℓ 7075 to SCC is closely related to the structure of grain boundary particles; the susceptibility to SCC decreases as the line fraction covered and mean particle size increase and as number of particles decreases.

- The processes involved in the matrix during the retrogression treatment mainly consist of:

  - dissolution of small η' particles
  - coarsening of all η variants
  - phase transformation of large η' particles to the η phase, particularly the η_2 and η_4 types
  - formation of η particles, particularly the η_1 variant

Meanwhile, the initial rapid coarsening of the particles characterizes the process occurring on grain boundaries during the retrogression treatment. The process occurring during the reaging treatment is believed to be essentially the re-precipitation of η' particles, frequently by heterogeneous nucleation.

- The beneficial effect of the RRA treatment on the susceptibility of 7075-T6 to SCC is believed to be due to the initial rapid coarsening of the particles on grain boundaries occurring during the retrogression treatment. This results in the increase of line fraction covered and the mean particle size, and in the decrease of number of particles per unit area. The high strength of the RRA structure, which is comparable to that of the T651 structure, is considered to arise from both the presence of many fine coherent η' particles and the high overall density of the precipitates.

References

1. L.F. Mondolfo, N.A. Gjøstein, and D.W. Levinson: Trans. AIME, 1956, Vol. 206, p. 1378.

2. R. Graf: Compt. Rend. Acad. Sci. (Paris), 1956, Vol. 242, p. 1311.

3. R. Graf: Compt. Rend. Acad. Sci. (Paris), 1956, Vol. 242, p. 2834.

4. R. Graf: Compt. Rend. Acad. Sci. (Paris), 1957, Vol. 244, p. 337.

5. R. Graf: J. Inst. Metals, 1957-58, Vol. 86, p. 535.

6. H. Schmalzried and V. Gerold: Z. Metallk., 1958, Vol. 49, p. 291.

7. G.W. Lorimer and R.B. Nicholson: The Mechanism of Phase Transformations in Crystalline Solids, p. 36, Inst. Metals, London, 1968.

8. G.W. Lorimer: Precipitation Process in Solids, ed. K.C. Russel and H.I. Aaronson, p. 109, TMS-AIME, Warrendale, PA, 1978.

9. F. Laves and J. Löhberg: Nachr. Akad. Wiss. (Göttingen), 1934, Vol. 1, p. 59.

10. J. Gjønnes and C.J. Simensen: Acta Met., 1970, Vol. 18, p. 881.

11. P.A. Thackery: J. Inst. Metals, 1968, Vol. 96, p. 228.

12. J.P. Embury and R.B. Nicholson: Acta Met., 1965, Vol. 13, p. 403.

13. A.J. DeArdo, Jr. and C.J. Simensen: Met. Trans., 1973, Vol. 4, p. 2413.

14. G. Thomas and J. Nutting: J. Inst. Metals, 1959-60, Vol. 88, p. 81.

15. G.W. Lorimer and R.B. Nicholson: Acta Met., 1966, Vol. 14, p. 1009.

16. D.W. Pashley, M.H. Jacobs, and J.T. Vietz: Phil. Mag., 1967, Vol. 16, p. 51.

17. J.H. Auld and S.M. Cousland: Scr. Met., 1971, Vol. 5, p. 765.

18. N. Ryum: Z. Metallk., 1975, Vol. 66, p. 338.

19. C.E. Lyman and J.B. Vander Sande: Met. Trans., 1976, Vol. 7A, p. 1211.

20. K.M. Dünkeloh, G. Kralik, and V. Gerold: Z. Metallk., 1974, Vol. 65, p. 291.

21. T. Ungár, J. Lendvai and I. Kovács: Aluminum, 1979, Vol. 55, p. 663.

22. G. Honyek, I. Kovács, J. Lendvai, N. Sinh, T. Ungár, H. Löffler, and R. Gerlach: J. Mater. Sci., 1981, Vol. 16, p. 2701.

23. H. Inoue, T. Sato, Y. Kojima and T. Takahashi: Met. Trans., 1981, Vol. 12A, p. 1429.

24. R.B. Nicholson, G. Thomas, and J. Nutting: J. Inst. Metals, 1958-59, Vol. 87, p. 429.

25. A. Kelly and R.B. Nicholson: Progr. Mater. Sci., 1963, Vol. 10, No. 3, p. 216.

26. A. Melander and P.A. Persson: Acta Met., 1978, Vol. 26, p. 267.

27. I. Kovács, J. Lendvai, T. Ungár, G. Groma, and J. Lakner: Acta Met., 1980, Vol. 28, p. 1621.

28. P.N. Adler, R. DeIasi, and G. Geschwind: Met. Trans., 1972, Vol. 3, p. 3191.

29. R. DeIasi and P.N. Adler: Met. Trans., 1977, Vol. 8A, p. 1177.

30. P.N. Adler and R. DeIasi: Met. Trans., 1977, Vol. 8A, p. 1185.

31. J.M. Papazian: NASC report RE-627, Gruman Aerospace Corporation, April 1981.

32. D.O. Sprowls and R.H. Brown: Metals Progr., 1962, Vol. 81, No. 4, p. 79.

33. D.O. Sprowls and R.H. Brown: Metals Progr., 1962, Vol. 81, No. 5, p. 77.

34. E.H. Dix, Jr.: "Edward de Mille Memorial Lecture in 1949," Trans. ASM, 1950, Vol. 42, p. 1057.

35. R.B. Mears, R.H. Brown, and E.H. Dix, Jr.: Symposium on "Stress Corrosion Cracking of Metals," p. 329, ASTM-AIME, 1944.

36. E.H. Dix, Jr.: Trans. AIME, 1940, Vol. 132, p. 11.

37. A.J. Sedriks, J.A.S. Green, and D.L. Novak: U.R. Evans Int. Conf. on Localized Corrosion, 1971, Williamsburg, Va., NACE.

38. A.J. Sedriks, J.A.S. Green, and D.L. Novak: Met. Trans., 1973, Vol. 4, p. 1992.

39. P.N.T. Unwin and R.B. Nicholson: Acta Met., 1969, Vol. 17, p. 1379.

40. K.G. Kent: J. Inst. Metals, 1969, Vol. 97, p. 127.

41. P.K. Poulouse, J.E. Morral, and A.J. McEvily: Met. Trans., 1974, Vol. 5, p. 1393.

42. R. Haag, J.E. Morral, and A.J. McEvily: Proc. Conf. on "Environmental

Degradation of Engineering Materials," p. 19, co-sponsored by NSF, held at Virginia Tech., VA, 1977.

43. C.J. Peel and P. Poole: Proc. Int. Conf. "Mechanism of Environment Sensitive Cracking of Materials," p. 147, Metals Soc., London, 1977.

44. K.G. Kent: J. Aust. Inst. Metals, 1970, Vol. 15, p.171.

45. B.V. Narasimha Rao: Met. Trans., 1980, Vol. 12A, p. 1356.

46. A.J. McEvily, J.B. Clark, and A.P. Bond: Trans. ASM., 1967, Vol. 60, p. 661.

47. A.J. Sedriks, P.W. Slattery, and E.N. Pugh: Trans. ASM, 1969, Vol. 62, p. 238.

48. A.J. DeArdo and R.D. Townsend: Met. Trans., 1970, Vol. 1, p. 2573.

49. P. Doig and J.W. Edington: Met. Trans., 1975, Vol. 6A, p. 943.

50. P. Doig and J.W. Edington: Corrosion, 1975, Vol. 31, p. 347.

51. P. Doig and J.W. Edington: Brit. Corros. J., Quarterly, 1974, Vol. 9, p. 461.

52. P. Doig, J.W. Edington, and G. Hibbert: Phil. Mag., 1973, Vol. 28, p. 971.

53. D.E. Ward and G.M. Lorimer: Proc. Int. Conf. on "Strength of Metals and Alloys," Inst. of Metals, London, 1973, Vol. 1, p. 488.

54. M. Raghavan: Met. Trans., 1980, Vol. 11A, p. 993.

55. J.M. Chen, T.S. Sun, R.K. Viswanadham, and J.A.S. Green: Met. Trans., 1977, Vol. 8A, p. 1935.

56. J.A.S. Green and W.G. Montague: Corrosion, 1975, Vol. 31, p. 209.

57. E.C. Pow, W.W. Gerberich, and L.E. Toth: Scr. Met., 1981, Vol. 15, p. 55.

58. R.K. Viswanadham, T.S. Sun, and J.A.S. Green; Met. Trans., 1980, Vol. 11A, p. 85.

59. R.J. Gest and A.R. Troiano: Corrosion, 1974, Vol. 30, p. 274.

60. L. Montgrain and P.R. Swann: Hydrogen in Metals, I.M. Bernstein and A.W. Thompson, eds., p. 575, ASM, Metals Park, OH, 1974.

61. M.O. Speidel: Hydrogen in Metals, I.M. Bernstein and A.W. Thompson, eds., p. 249, ASM, Metals Park, OH, 1974.

62. G.M. Scamans, R. Alani, and P.R. Swann: Corrosion Sci., 1976, Vol. 16, p. 443.

63. B. Cina and B. Ranish: "New Technique for Reducing Susceptibility to Stress Corrosion of High-Strength Aluminum Alloy," Israel Aircraft Industries, Ltd., Israel, unpublished work.

64. B. Cina: Int. Conf. on "Aluminum Industrial Products Proceedings," ASM, Pittsburgh, October 1974.

65. B. Cina: "2nd Israel-Norwegian Technical and Scientific Symposium, Electrochemistry and Corrosion," Norway, June 1978.

66. Interdepartmental Communication, Lockheed Aircraft Co., CA.

67. H.E. Chandler and D.F. Baxter: "Technology Forecast '80 - Trends in Nonferrous Metal Technology," Metal Progr., 1980, Vol. 117, No. 1, p. 33.

68. H.E. Chandler: "Challenges in Aerospace Materials and Processes During the '80's," Metal progr., 1980, Vol. 117, No. 4, p. 41.

69. R.S. Kaneko: Metal Progr., 1980, Vol. 117, No. 5, p. 41.

70. R.E. Swanson, I.M. Bernstein, and A.W. Thompson: Scr. Met., 1982, Vol. 16, p. 321.

71. P.H. Hirsch, A. Howie, R.B. Nicholson, D.W. Pashley, and M.J. Whelan: Electron Microscopy of Thin Crystals, p. 188, Butterworths, London, 1965.

72. H.Y. Hunsicker: Aluminum I, p. 109, ASM, Metals Park, OH, 1967.

73. C.A. Johnson: Surf. Sci., 1965, Vol. 3, p. 429.

74. A.J. Ardell and R.B. Nicholson: Acta Met., 1966, Vol. 14, p. 1295.

75. H.P.K. Kirchner: Met. Trans., 1971, Vol. 2, p. 2861.

TABLE 1

	T651	RRA30	R30	T76	RRA10	RRA60
η' Plate*	50x15Å	62x15Å	≤ 50Å	65Å	50Å	65Å
η' Spherical	≤ 50Å	≤ 50Å	≤ 50Å		≤ 50Å	≤ 50Å
	Very Many	Many	Some	Some	Very Many	Some
η_1 Plate	116x20Å	138x30Å	125x30Å	130x50Å	128X30Å	142x50Å
	Some	Some	Some	Many	Some	Many
η_2 Plate	110x20Å	114x30Å	112x30Å	136x50Å	115x20Å	138x50Å
	Few	Some	Some	Many	Some	Many
η_4 Lath**	125Å	152Å	164Å	202x100Å	100Å	208x75Å
	Very Few	Few	Few	Few	Few	Some
$\bar{d}$ (overall)	69Å	77Å	97Å	107Å	72Å	119Å
$x10^{-3}/\mu m^2$ N(Overall)	1.02 ± 0.13	1.04 ± 0.15	0.37 ± 0.10	0.55 ± 0.08	1.26 ± 0.10	0.99 ± 0.18

* diameter x thickness, ** length x diameter

Table 2

	$N_A(x10^{-2}/\mu m^2)$	$L_A(\%)$	$A_A(\%)$	$\bar{d}(\mathring{A})$	PFZ($\mathring{A}$)	
					ST-L	L-T
T651	5.0 ± 0.7	13.8 ± 0.7	13.4 ± 2.0	267	538±12.5	466±49
RRA 10	3.4 ± 0.7	18.2 ± 5.2	16.8 ± 4.6	338		
RRA 30	3.3 ± 1.2	19.3 ± 3.7	17.1 ± 3.8	435	540 ± 97	
RRA 60	3.0 ± 0.8	21.8 ± 4.1	17.8 ± 3.0	446		
T76	3.3 ± 0.6	24.3 ± 4.7	22.9 ± 7.4	477	596 ± 40	

Figure Captions

Fig. 1 Hardness vs. immersion time at the retrogression temperature, 240°C. o retrogressed and reaged 7075-T651, • retrogressed 7075-T651.

Fig. 2 Specimen temperature vs. immersion time at 240°C.

Fig. 3 Bright-field micrographs of samples in various temper conditions. (a) T651, (b) T76, (c) RRA-30, (d) R-30.

Fig. 4 Diffraction patterns of samples in various tempers for B = [112]. (a) T651, (b) T76, (c) RRA-30, (d) R-30.

Fig. 5 Schematic diagram of the diffraction pattern for B = [$\bar{1}$12] including frequently observed strong spots. ◉ $[\bar{1}12]_{A\ell}$, o η', ⊙ η_1, • η_2, + η_4.

Fig. 6 Diffraction patterns of samples in various tempers for B = [011] and B = [001]. (a) T651; B = [011], (b) T651; B = [001], (c) T76; B = [011], (d) T76; B = [001], (e) RRA-30; B = [011], (f) R-30; B = [011].

Fig. 7 Schematic diagram of the expected diffraction pattern for B = [001] including doubly diffracted spots. Indices of each reflection only indicate its type. ◉ $[001]_{A\ell}$, oη', ⊙ η_1, • η_2, + η_4.

Fig. 8 Schematic diagrams illustrating the possible formation of oxide spots of γ-$A\ell_2O_3$ at the intersection of its multiple ring patterns of strongly diffracting planes {220}, {311}, {400}, and {440}, due to the double diffraction effect, in three different zone axes, B = [001], B = [011], and B = [112]. ◉ matrix spots, ∘ oxide spots.

Fig. 9 Diffraction patterns of T651 samples, prepared by ion milling. (a) B = [112], (b) B = [011].

Fig. 10 Diffraction patterns of retrogressed and reaged samples for 10 and 60 s of immersion time. (a) RRA-10; B = [112], (b) RRA-10; B = [011], (c) RRA-60; B = [112], (d) RRA-60; B = [011].

Fig. 11 Dark-field micrographs of the RRA-30 structure. (a), (b) Images obtained using the $(20.0)\eta' + (\bar{1}2.0)\eta_4$ and $(12.0)\eta_1$ reflections, respectively, in B = [011]. (c), (d), (e), (f) Images obtained in B = [$\bar{1}$12] using the $(20.0)\eta' + (00.4)\eta_1 + (20.0)\eta_2 + (00.4)\eta_4$, $(20.2)\eta' + (02.2)\eta_1 + (20.1)\eta_2$, $(\bar{1}2.0)\eta_1$, and $(\bar{1}2.2)\eta_4 + (10.5)\eta'$ reflections, respectively. (g), (h) Dark-field image formed with the $(00.4)\eta' + (\bar{1}2.0)\eta_4$ reflections, and the corresponding bright-field image.

Fig. 12 Dark-field micrographs of the T651 structure. (a), (b), (c), (d) Images obtained using the $(10.5)\eta' + (\bar{1}2.2)\eta_4 + (10.3)\eta_2$, $(20.0)\eta' + (00.4)\eta_1 + (20.0)\eta_2 + (00.4)\eta_4$, $(01.1)\eta_1 + (10.1)\eta'$, and $(00.2)\eta_2$ reflections respectively. (e), (f) Dark-field image formed with the $(00.8)\eta'$ reflection and the corresponding bright-field image.

Fig. 13 Dark-field micrographs of the T76 structure. (a), (b), (c), (d) Images obtained using the $(20.0)\eta' + (00.4)\eta_1 + (20.0)\eta_2 + (00.4)\eta_4$, $(\bar{1}2.0)\eta_1 + (20.0)\eta_2$, $(\bar{1}2.0)\eta_4$ and $(10.5)\eta' + (10.3)\eta_2 + (\bar{1}2.2)\eta_4$ reflections, respectively.

Fig. 14 Dark-field micrographs of the R-30 samples. (a), (b) Images obtained using the $(00.2)\eta' + (00.2)\eta_2 + (\bar{1}2.0)\eta_4$ and $(20.2)\eta' + (20.1)\eta_2 + (02.2)\eta_1$ reflections, respectively.

Fig. 15 Dark-field micrographs of RRA-10 samples. (a), (b) Images obtained using the $(20.0)\eta' + (00.4)\eta_1 + (20.0)\eta_2 + (00.4)\eta_4$ and $(20.2)\eta' + (02.2)\eta_1 + (20.1)\eta_2$ reflections, respectively.

Fig. 16 Dark-field micrographs of RRA-60 samples. (a), (b), (c) Images obtained using the $(20.0)\eta' + (00.4)\eta_1 + (20.0)\eta_2 + (00.4)\eta_4$, $(\bar{1}2.0)\eta_1 + (20.0)\eta_2$, and $(10.5)\eta' + (10.3)\eta_2 + (\bar{1}2.2)\eta_4$ reflections, respectively.

Fig. 17 Overall size distribution of particles in the matrix in various temper conditions, T651, T76, RRA-30, R-30, RRA-10, and RRA-60.

Fig. 18 Variation of the overall mean particle size, $\bar{d}$, and particle number per unit area, N, in the matrix as a function of immersion time at the retrogression temperature, 240°C. ◉ particle size, Δ particle density.

Fig. 19 Precipitate free zones in various temper conditions. (a) T651 (ST-L) orientation), (b) T651 (L-T orientation), (c) RRA-30, (d) T76.

Fig. 20 Bright-field image showing grain boundary precipitates in a RRA-30 sample (a) and corresponding diffraction pattern for B = [112] (b). (c), (d) Dark-field images obtained using the $(20.0)\eta' + (00.4)\eta_1 + (20.0)\eta_2 + (00.4)\eta_4$ and $(20.0)\eta_2 + (\bar{1}2.0)\eta_1$ reflections, respectively, taken from the same region of the foil as (a).

Fig. 21 Bright-field images of precipitates on grain boundaries of samples in various temper conditions. (a) T651, (b) RRA-30, (c) R-30, (d) T76, (e) RRA-10, (f) RRA-60.

Fig. 22 Size distribution of particles on grain boundaries in samples in various temper conditions, T651, T76, RRA-30, R-30, RRA-10, and RRA-60.

Fig. 23 Variation of particle structures on grain boundaries as a function of immersion time at the retrogression temperature, 240°C. O line fraction (L_A), ◉ mean particle size ($\bar{d}$), Δ particle density ($N_A/\mu m^2$). Their values in the T76 structure are also shown.

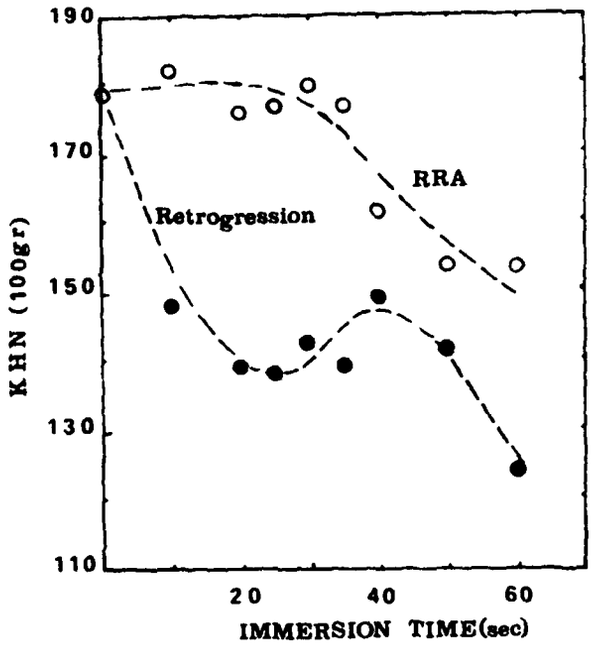
190
170
150
130
110
KHN (100gr)
RRA
Retrogression
20
40
60
IMMERSION TIME(sec)

Fig.1

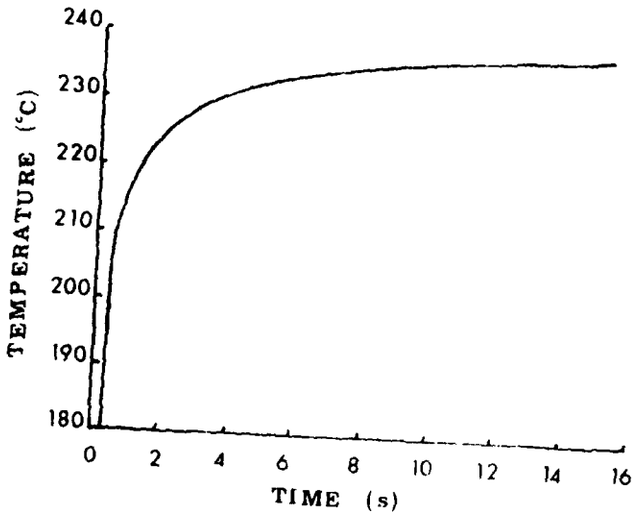
240
230
220
210
200
190
180
TEMPERATURE (°C)
0
2
4
6
8
10
12
14
16
TIME (s)

Fig. 2

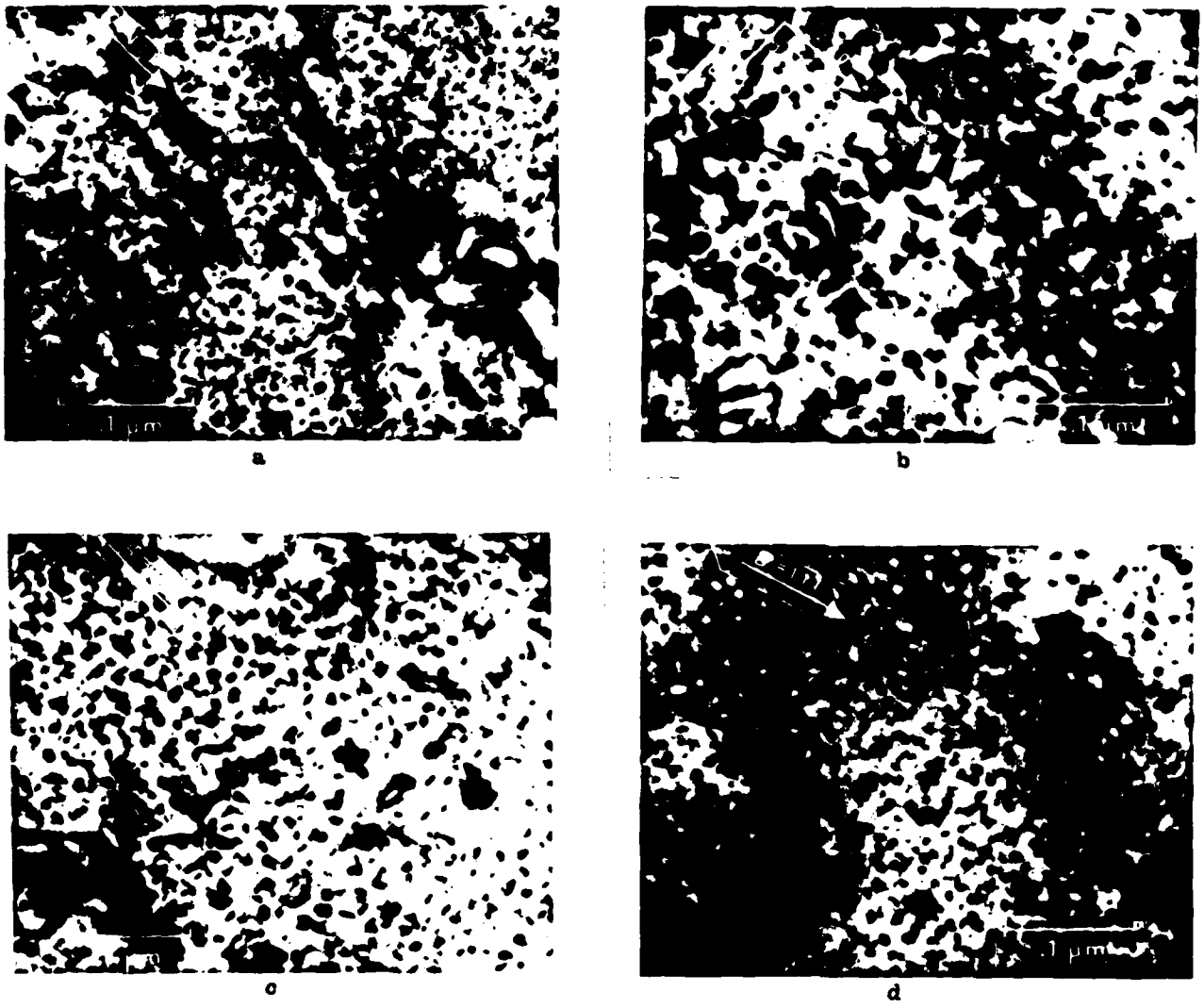

Fig.3

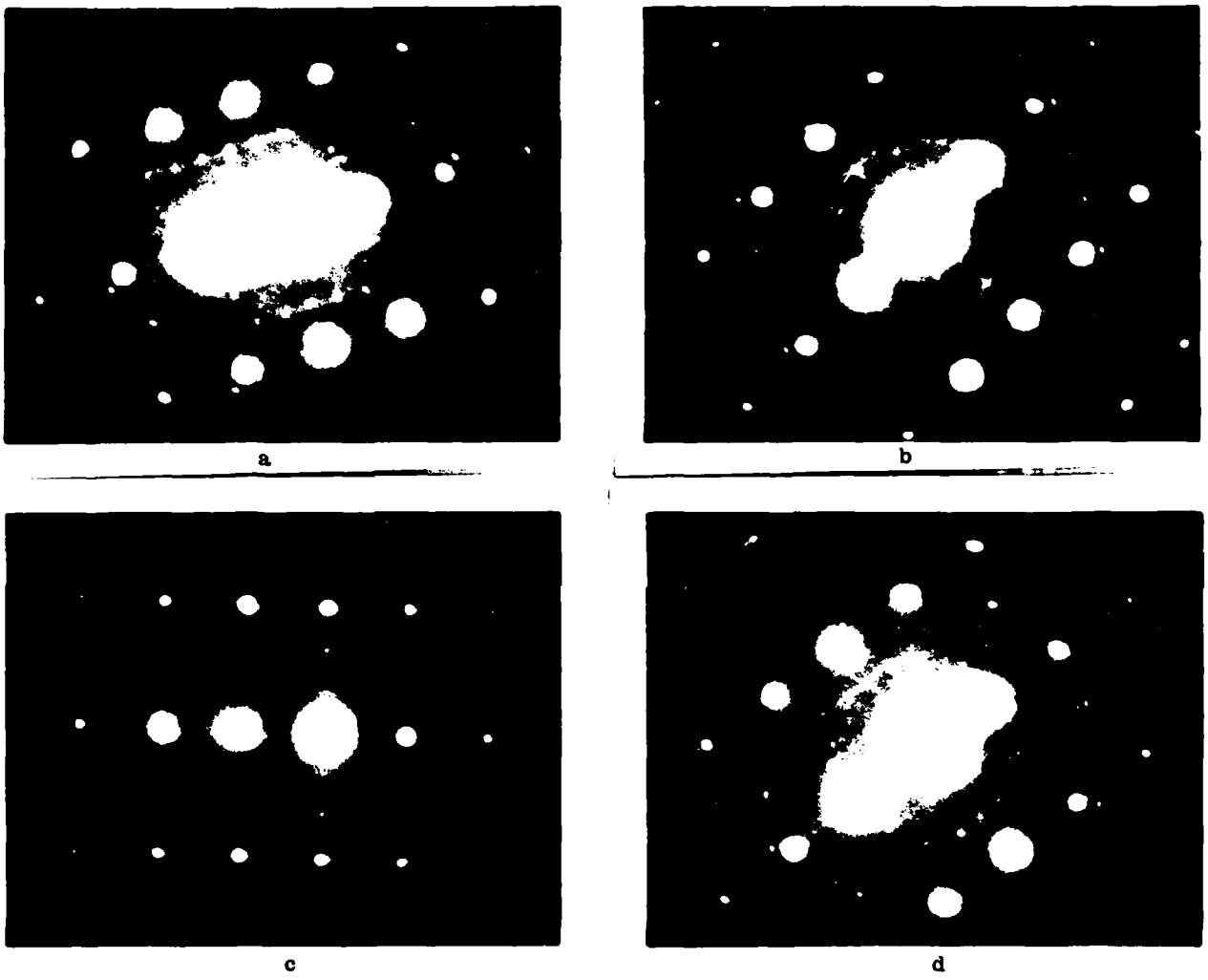

Fig.4

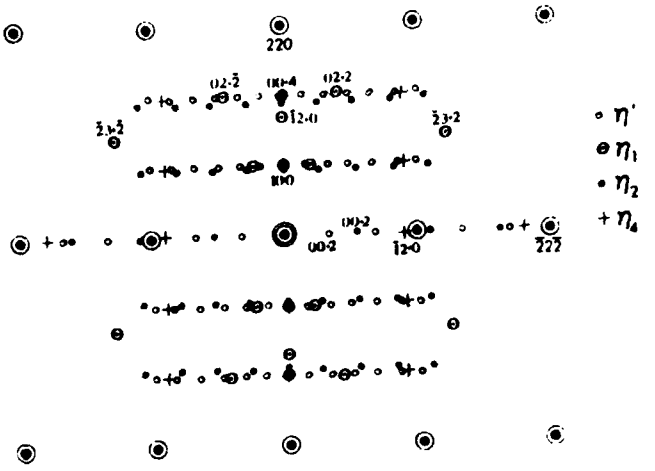

Fig.5

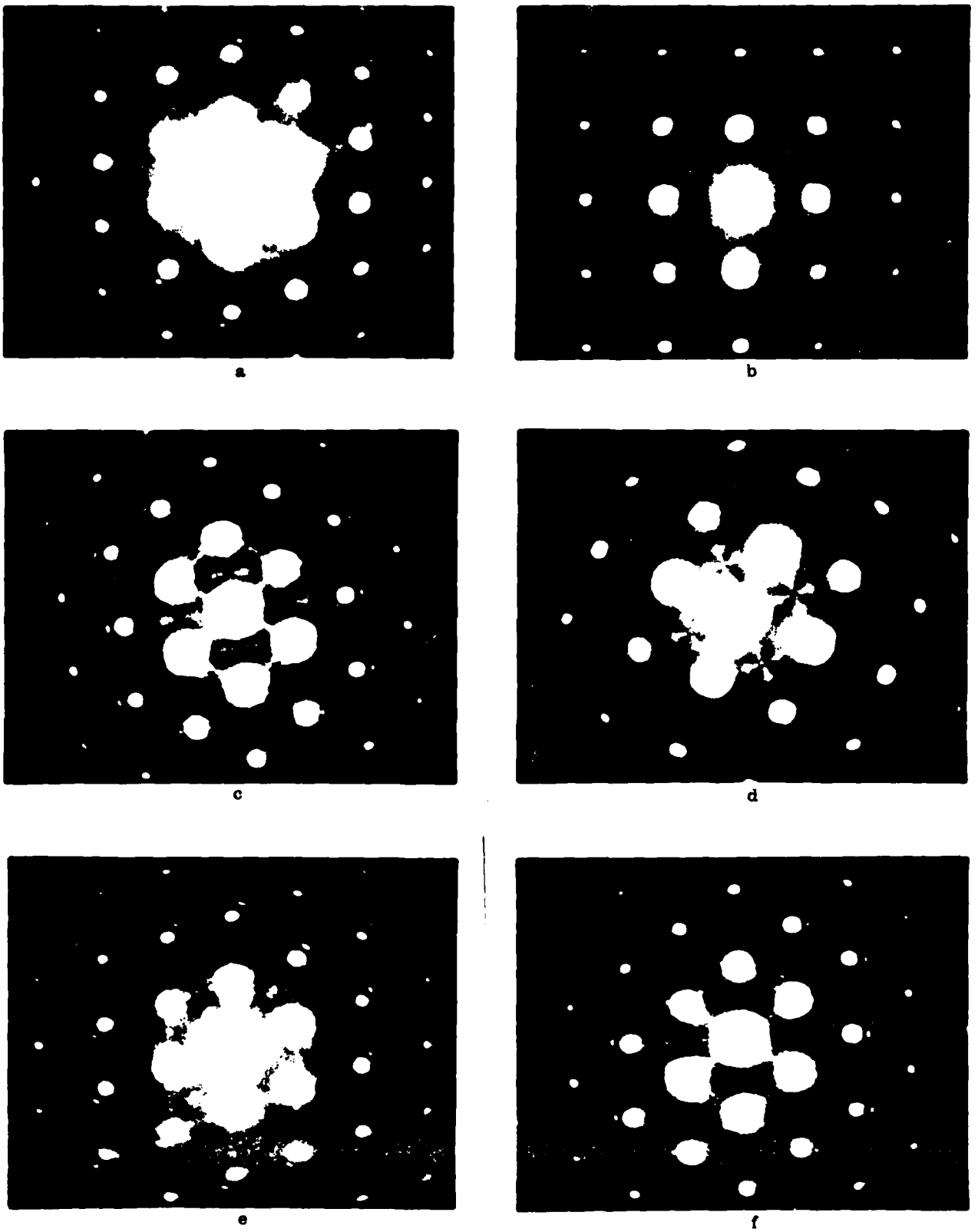

Fig. 6

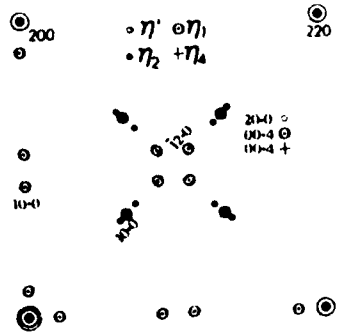

Fig.7

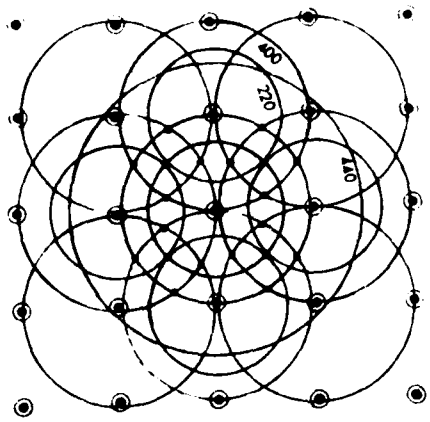

B[001]

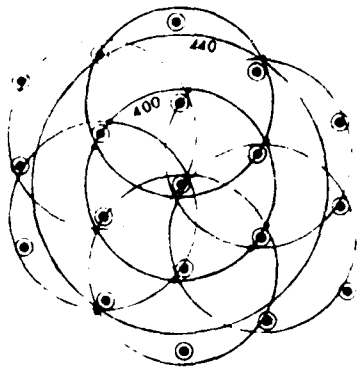

B[011]

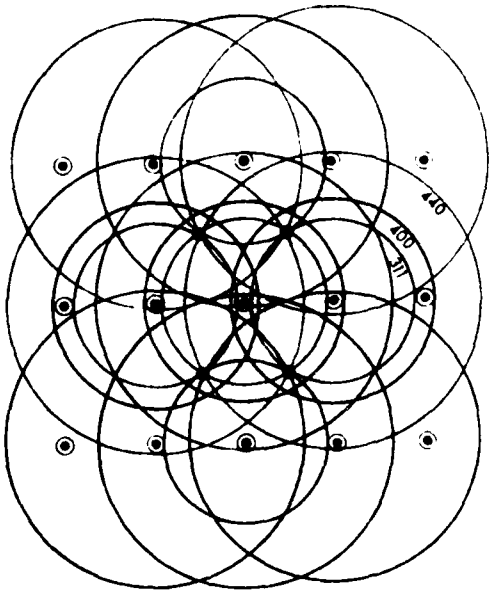

B[112]

Fig. 8

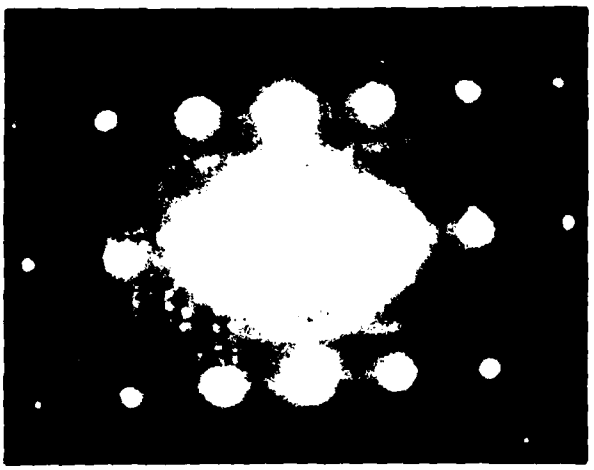

a

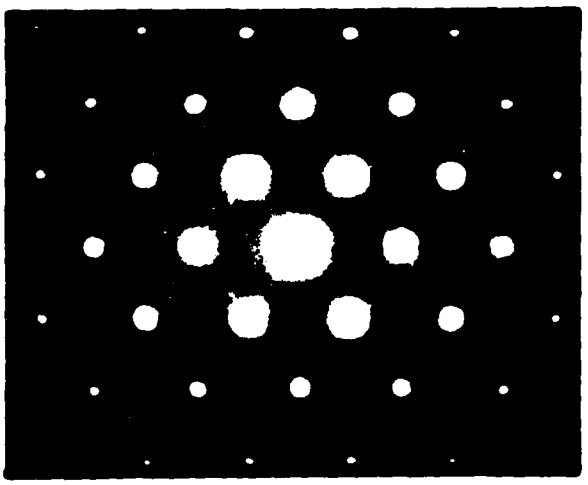

b

Fig. 9

a

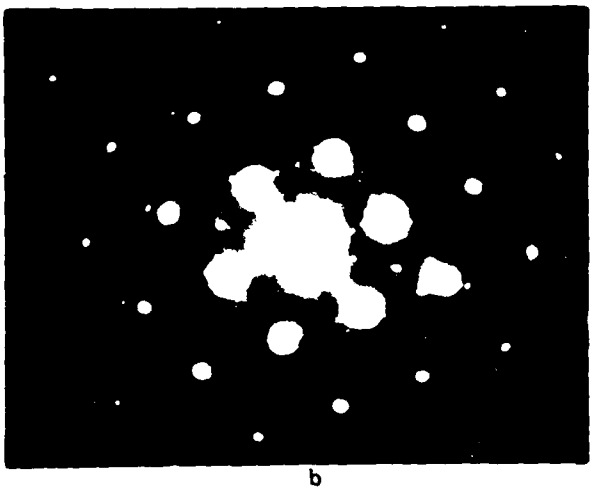

b

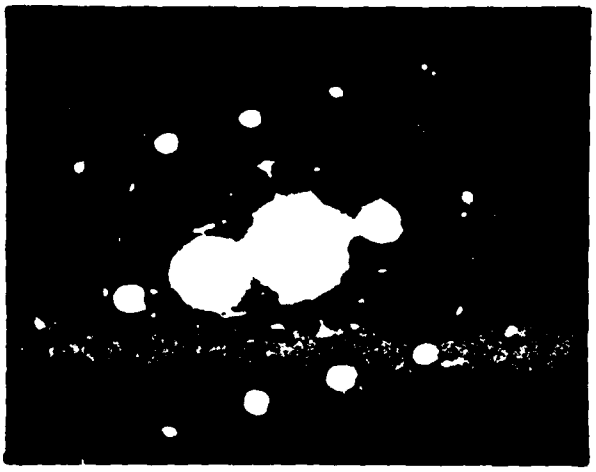

c

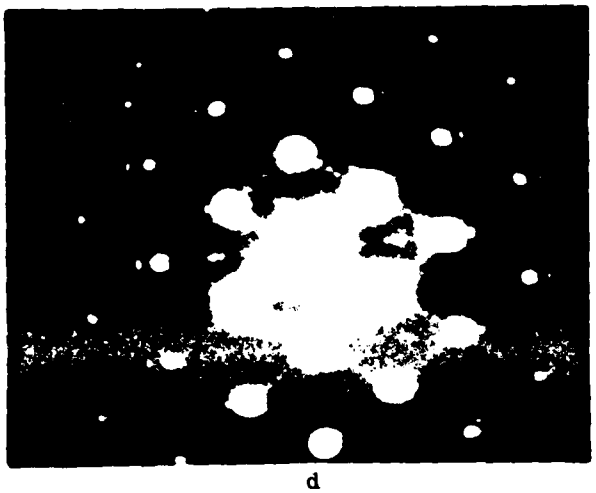

d

Fig. 10

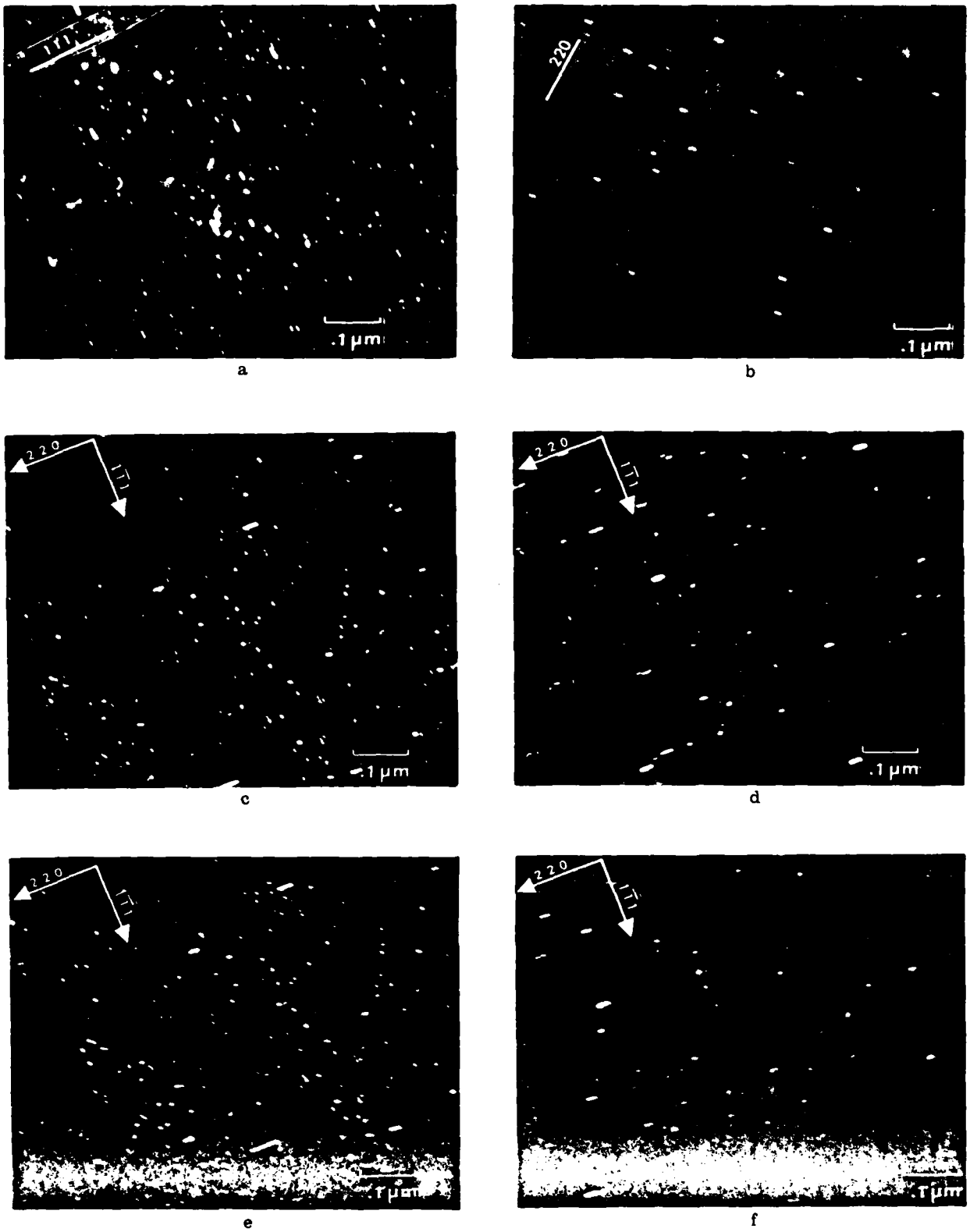
111
.1 μm
a
220
.1 μm
b
220
1̄1̄1
.1 μm
c
220
1̄1̄1
.1 μm
d
220
1̄1̄1
.1 μm
e
220
1̄1̄1
.1 μm
f

Fig.11

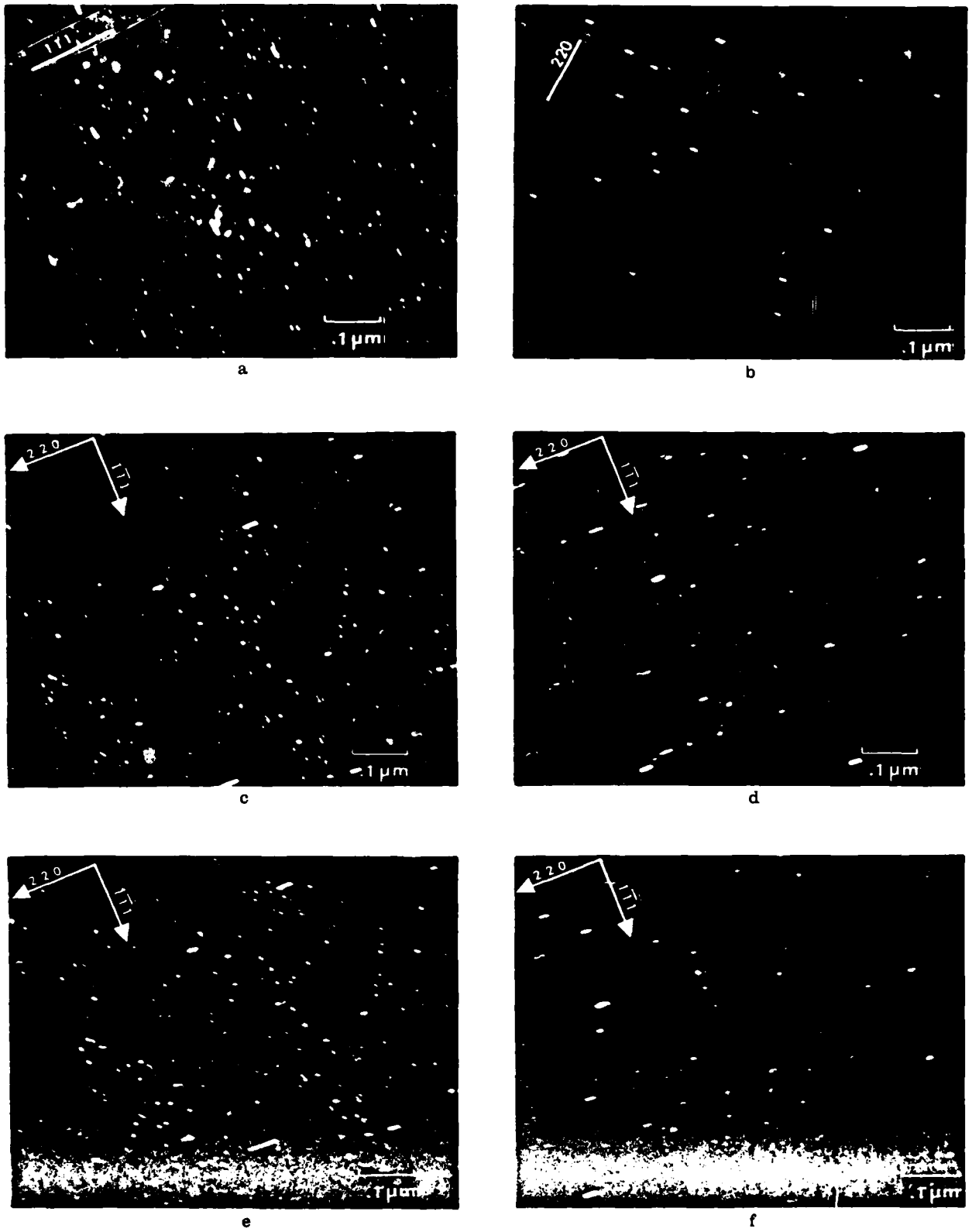
111
.1 μm
a
220
.1 μm
b
220
1̄1̄1
.1 μm
c
220
1̄1̄1
.1 μm
d
220
1̄1̄1
.1 μm
e
220
1̄1̄1
.1 μm
f

Fig.11

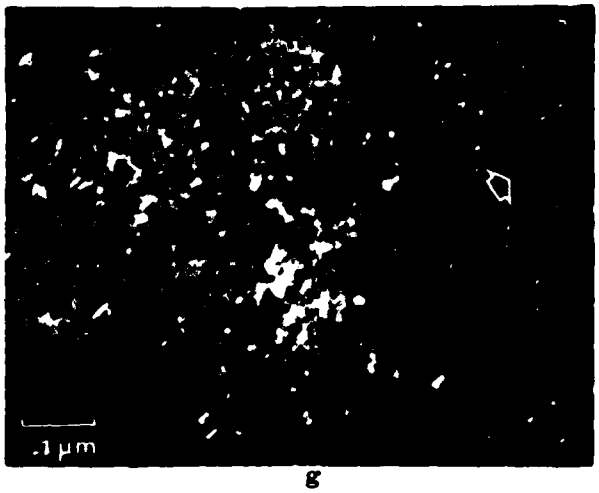

g

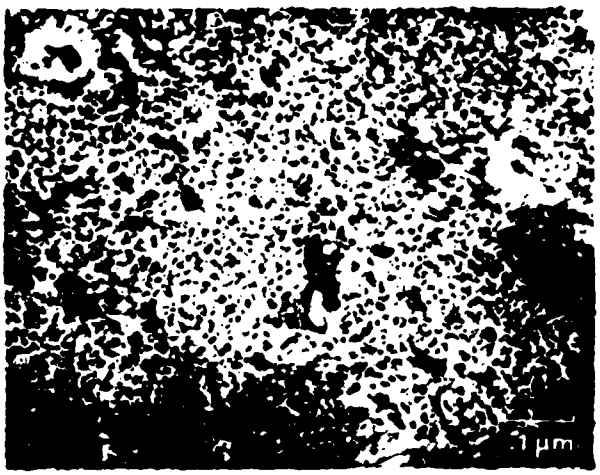

h

Fig.11

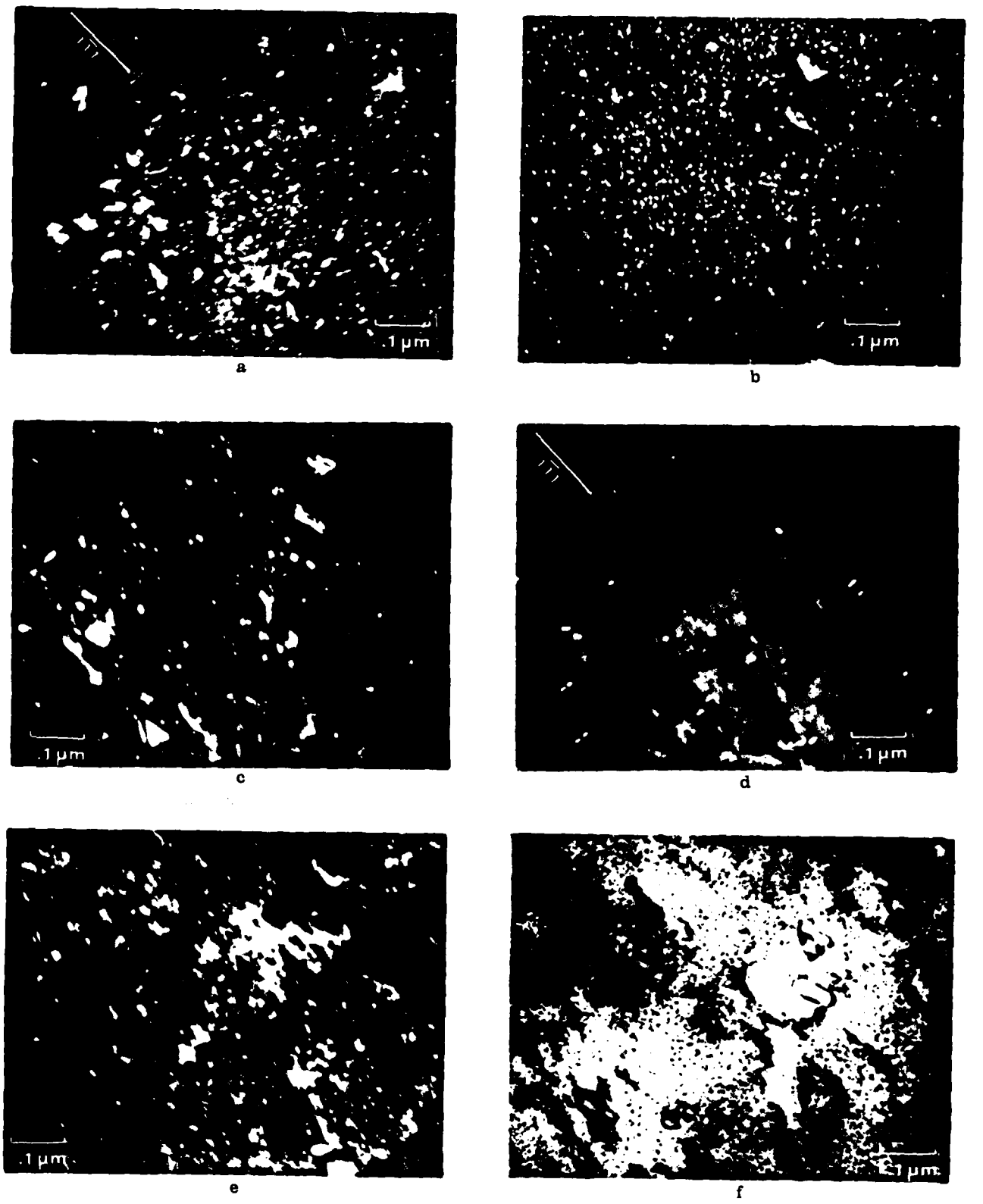

Fig.12

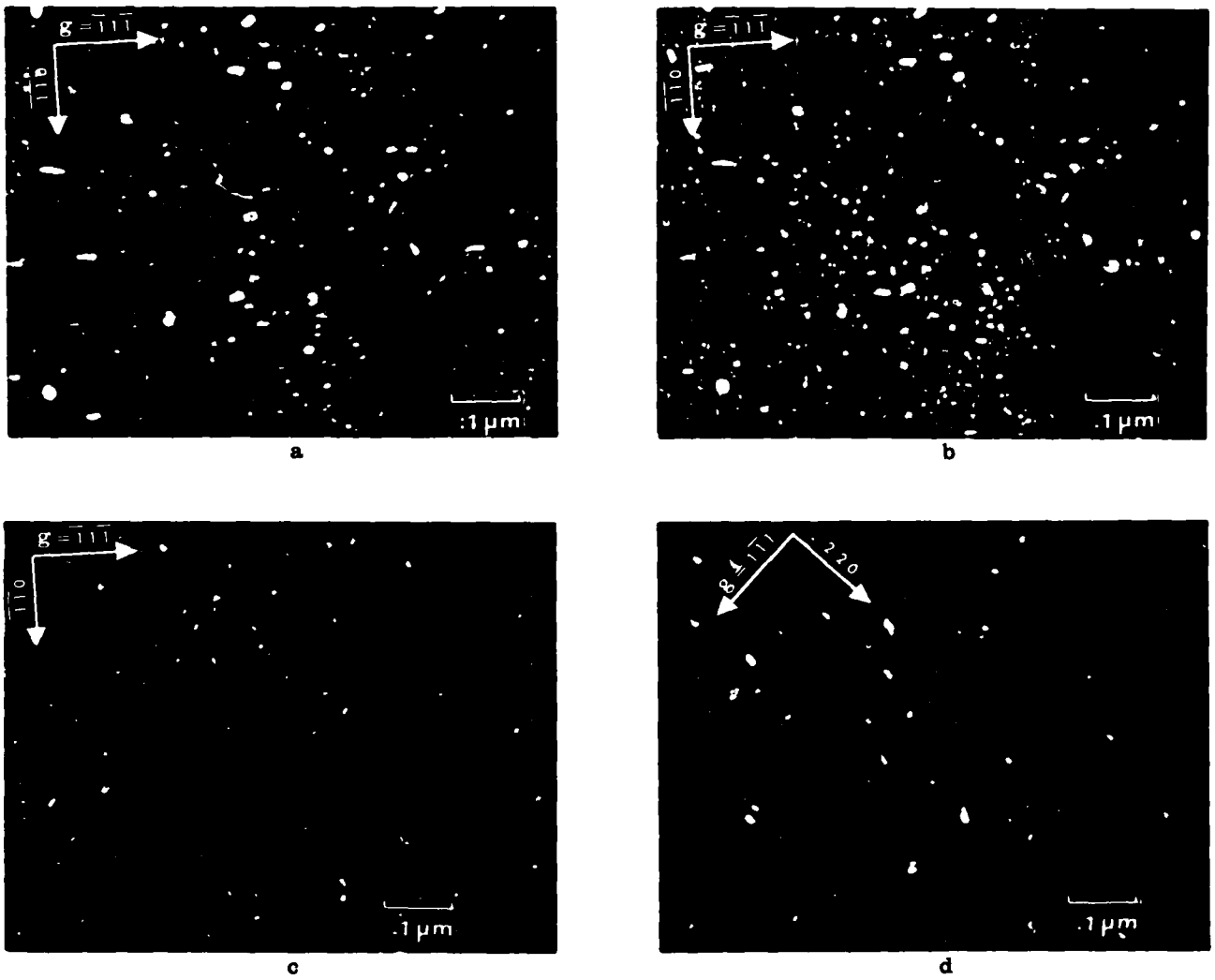
g = $\bar{1}\bar{1}\bar{1}$
$\bar{1}\bar{1}0$
.1 μm
a
g = $\bar{1}\bar{1}\bar{1}$
$\bar{1}\bar{1}0$
.1 μm
b
g = $\bar{1}\bar{1}\bar{1}$
$\bar{1}\bar{1}0$
.1 μm
c
g ≠ $\bar{1}\bar{1}\bar{1}$
2 2 0
.1 μm
d

Fig.13

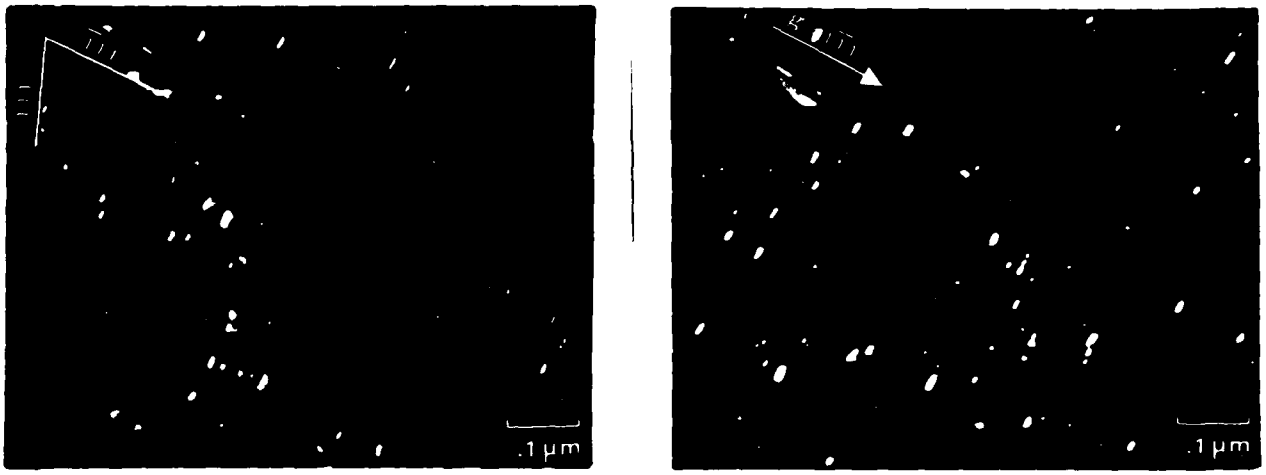

a b

Fig.14

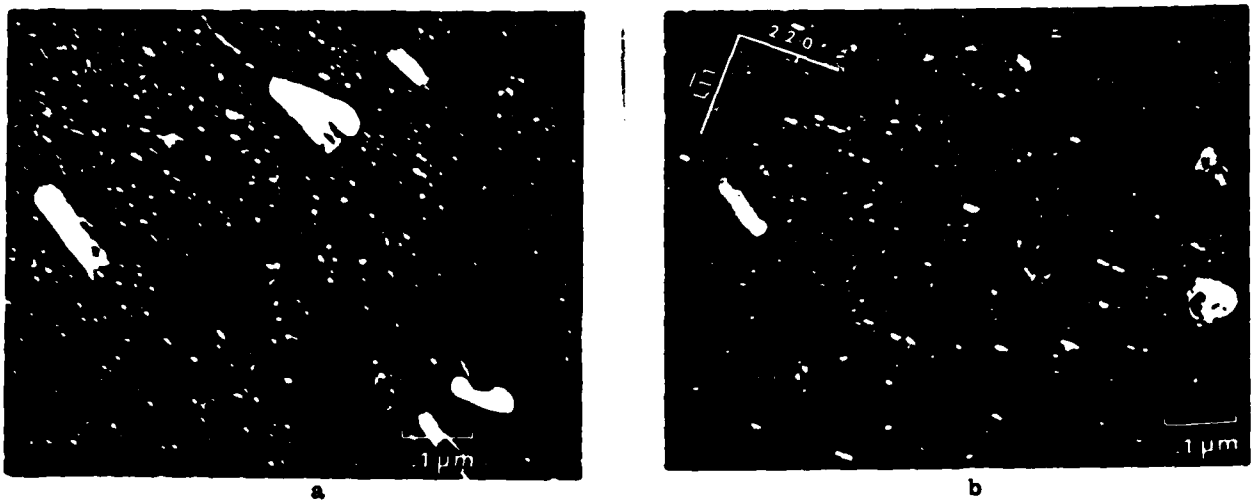

a b

Fig.15

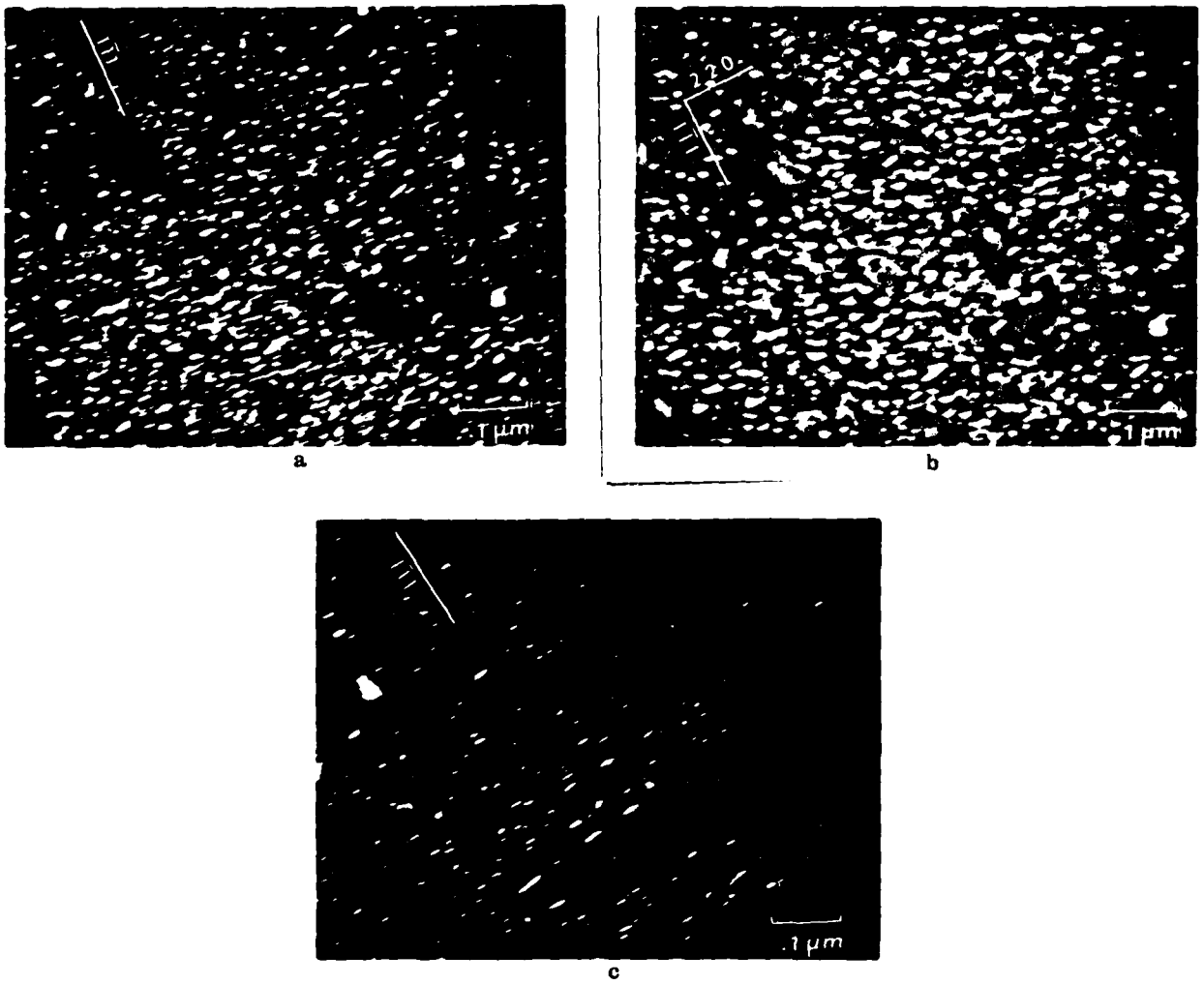

Fig.16

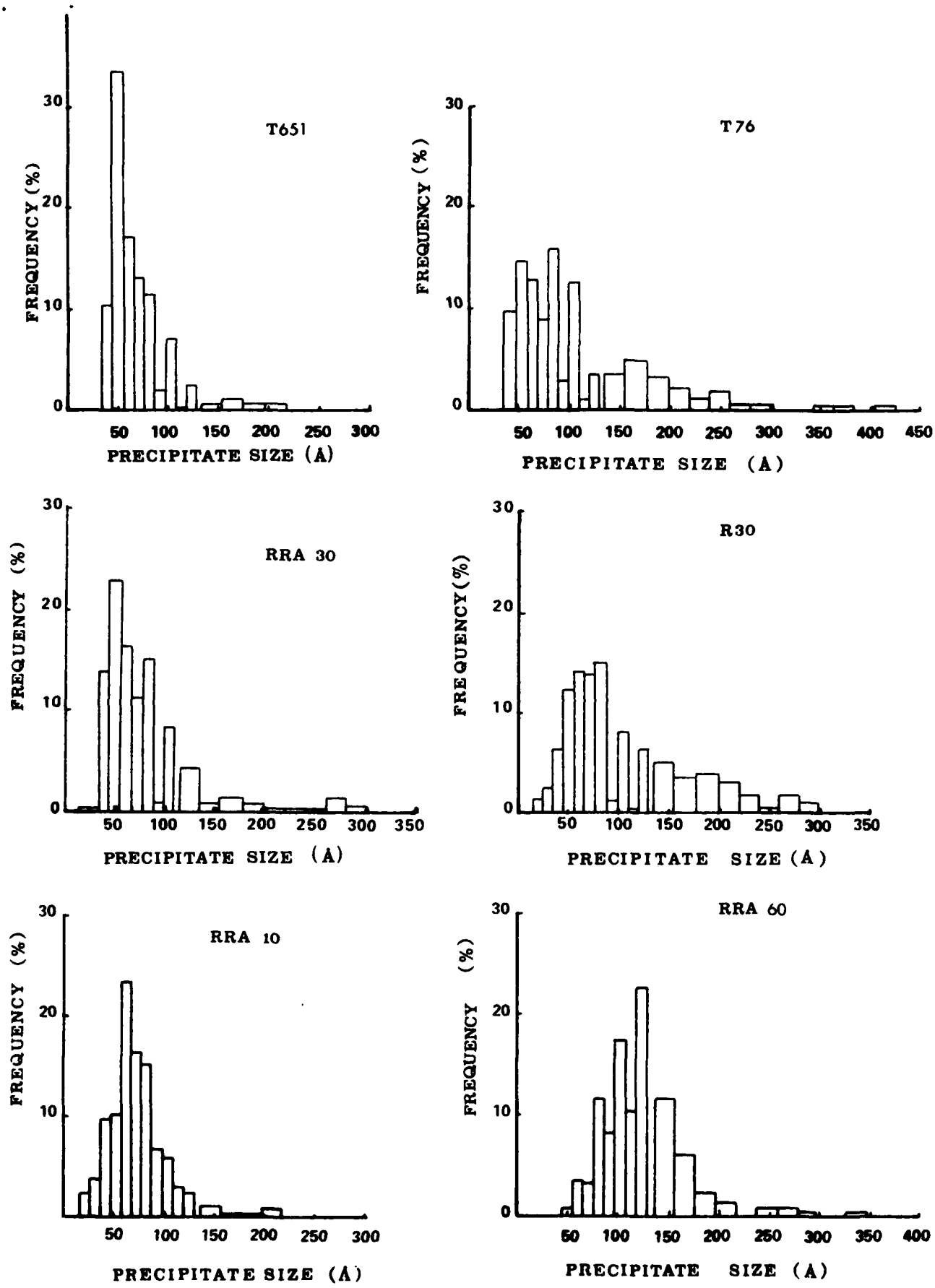
T651
FREQUENCY (%)
PRECIPITATE SIZE (Å)
T76
FREQUENCY (%)
PRECIPITATE SIZE (Å)
RRA 30
FREQUENCY (%)
PRECIPITATE SIZE (Å)
R30
FREQUENCY (%)
PRECIPITATE SIZE (Å)
RRA 10
FREQUENCY (%)
PRECIPITATE SIZE (Å)
RRA 60
FREQUENCY (%)
PRECIPITATE SIZE (Å)

Fig.17

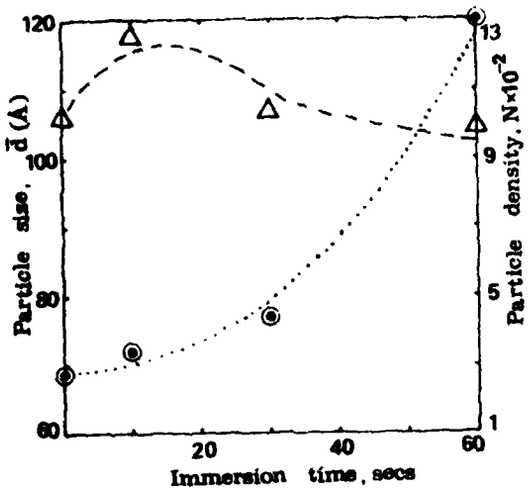
120
100
80
60
Particle size, $\bar{d}$ (Å)
13
9
5
1
Particle density, N×10^{-2}
20
40
60
Immersion time, secs

Fig.18

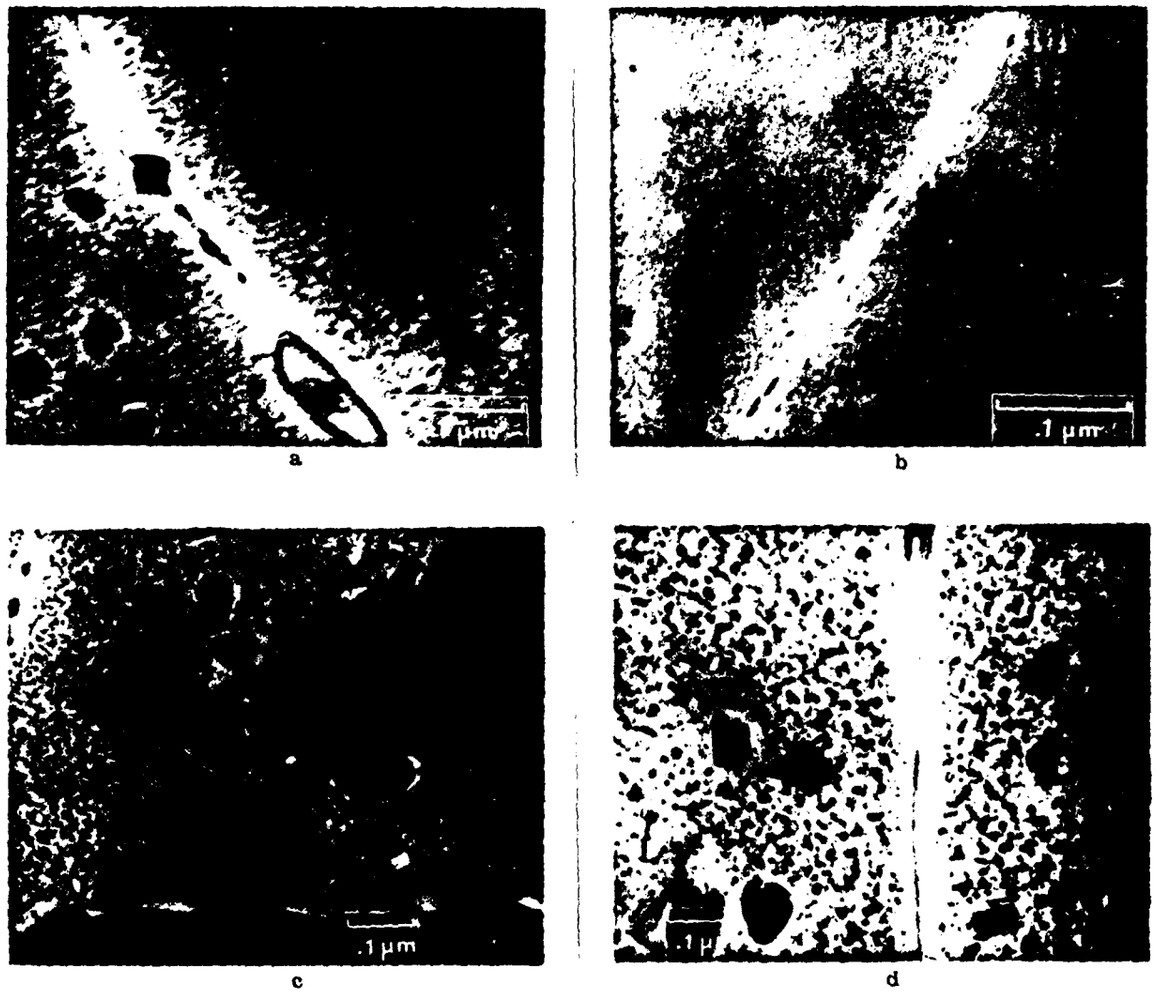

Fig.19

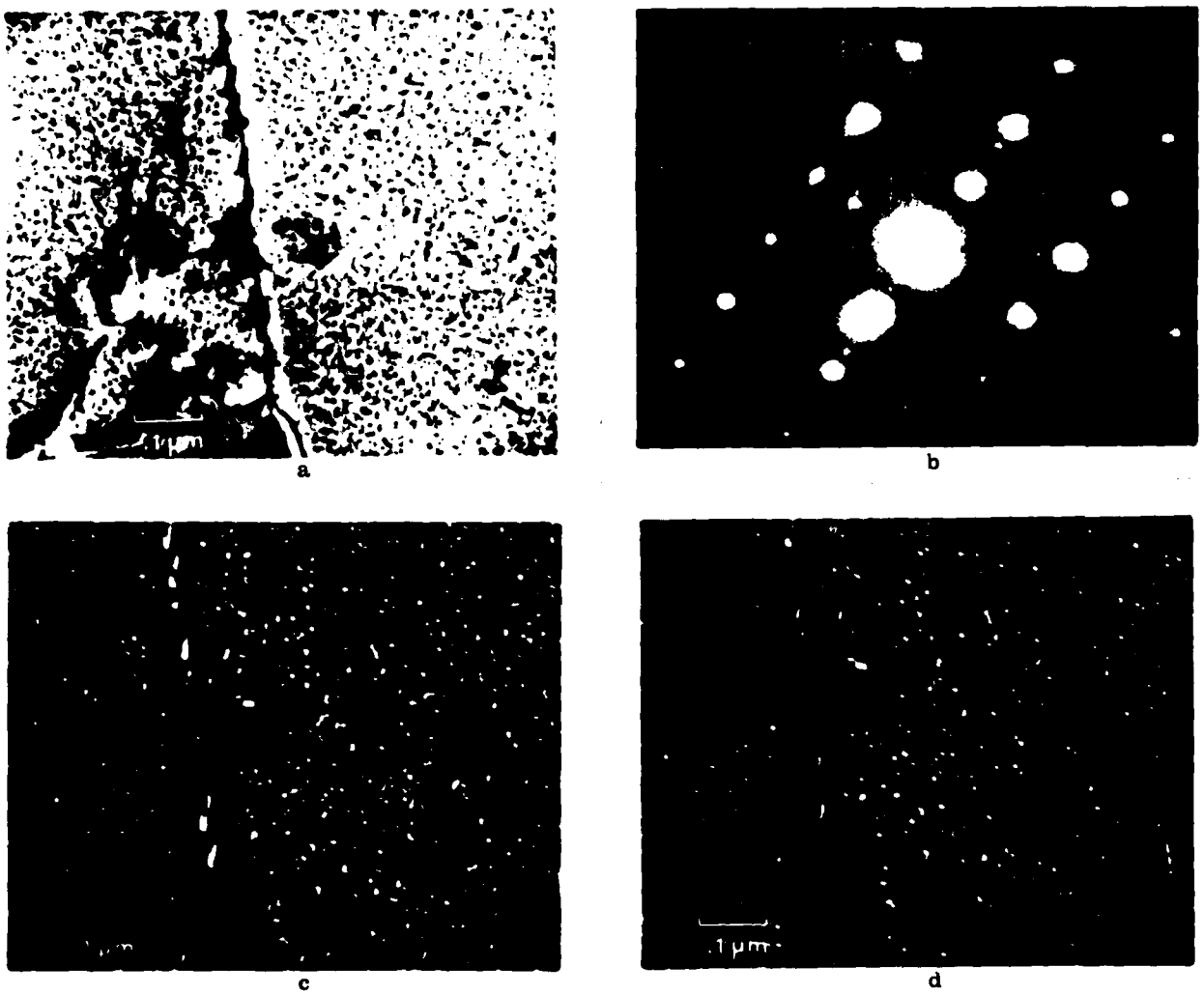

Fig. 20

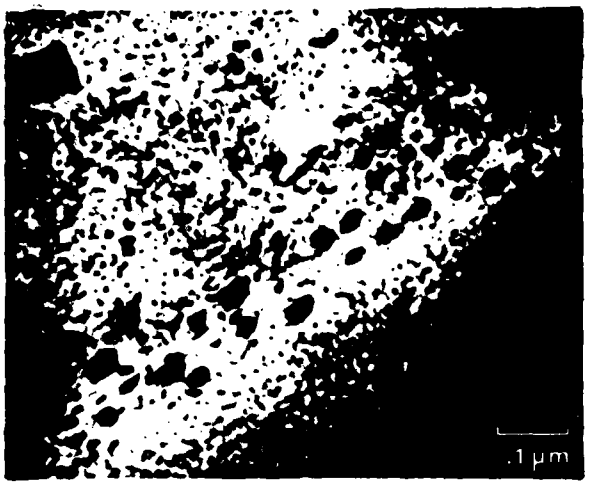

a

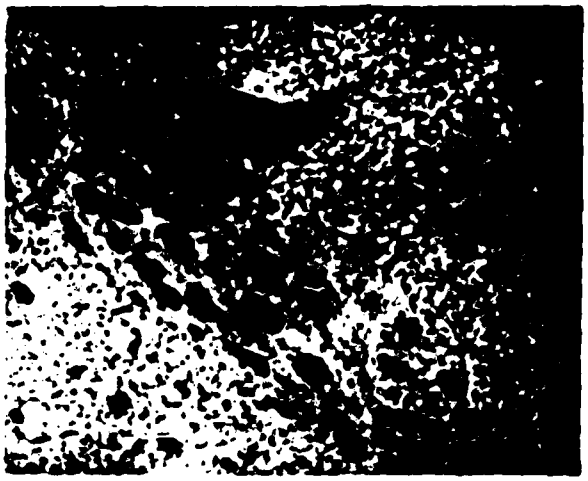

b

c

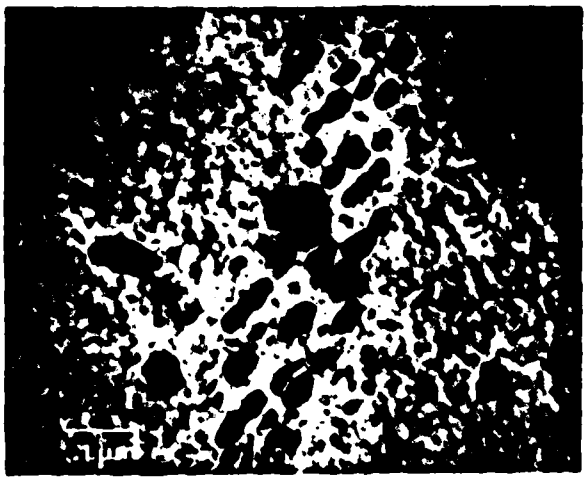

d

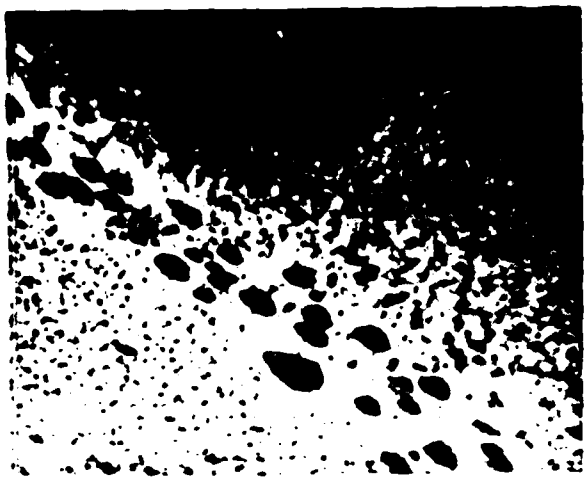

e

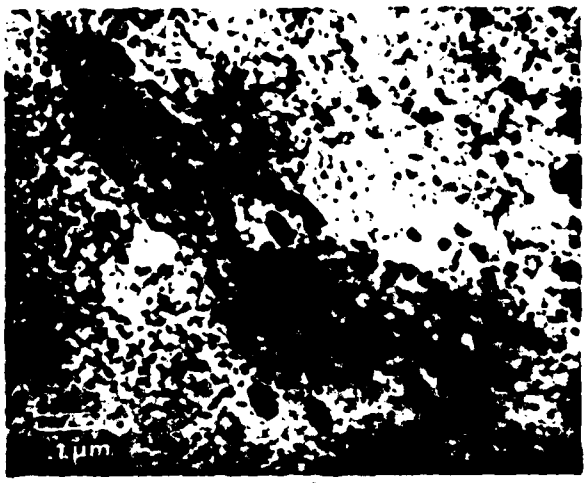

f

Fig.21

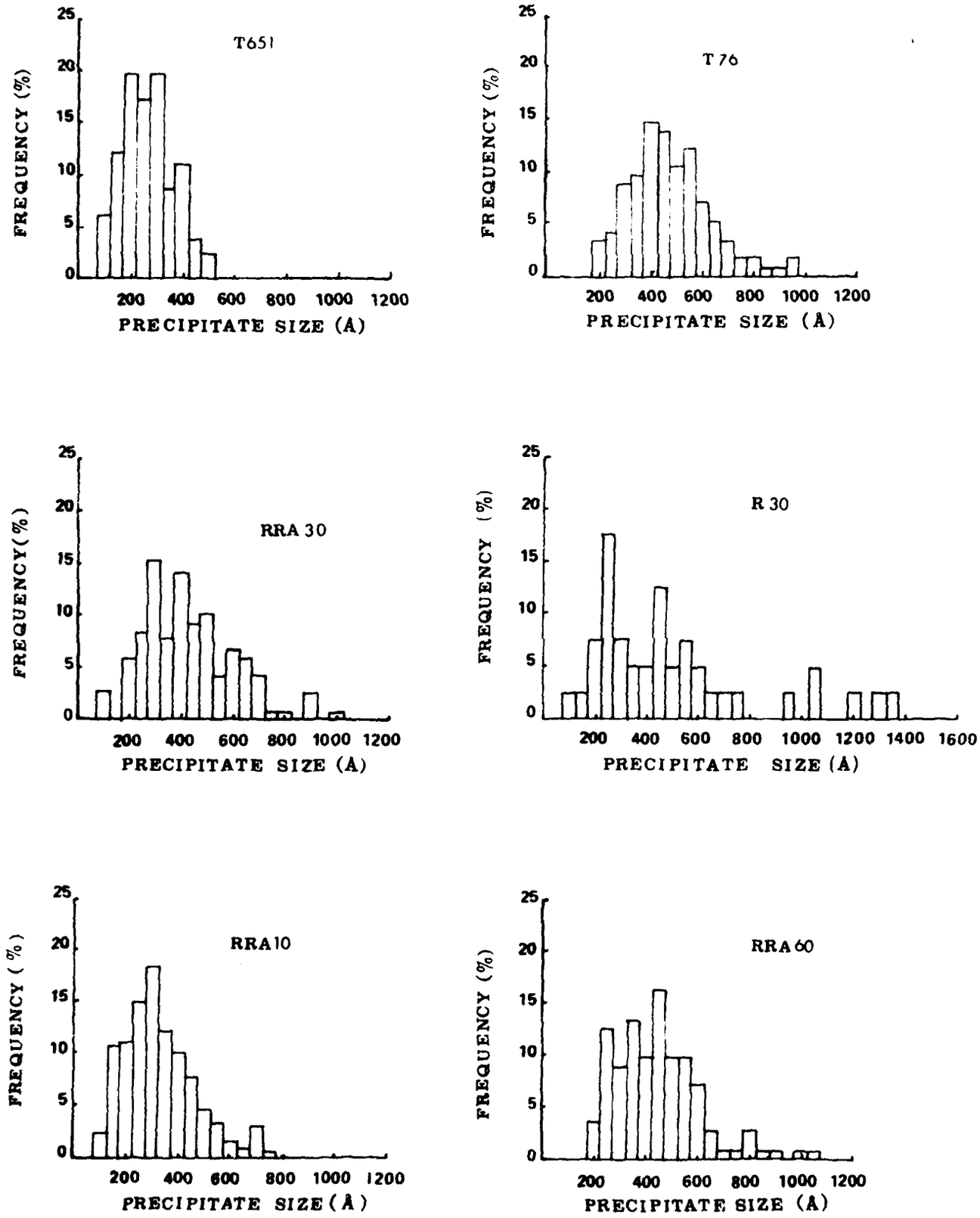
T651
T76
RRA 30
R 30
RRA10
RRA60
FREQUENCY (%)
PRECIPITATE SIZE (Å)
0
5
10
15
20
25
200
400
600
800
1000
1200
1400
1600

Fig.22

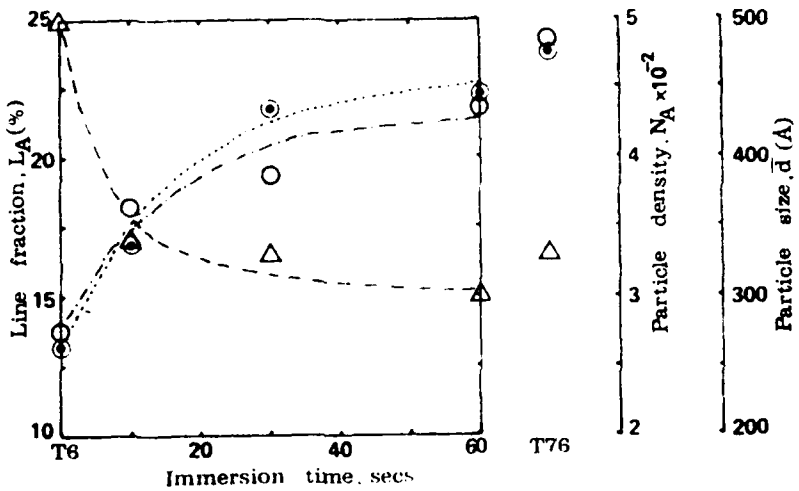
25
20
15
10
Line fraction, L_A(%)
T6
20
40
60
T76
Immersion time, secs
5
4
3
2
Particle density, $N_A \times 10^{-2}$
500
400
300
200
Particle size, $\bar{d}$ (Å)

Fig.23

DATE
FILMED

9-8